Title: The complex dynamics of the 2023 Kahramanmaraş, Turkey, M_w 7.8-7.7 earthquake doublet

Authors: Zhe Jia[1*], Zeyu Jin[1], Mathilde Marchandon[2], Thomas Ulrich[2], Alice-Agnes Gabriel[1,2], Wenyuan Fan[1], Peter Shearer[1], Xiaoyu Zou[1], John Rekoske[1], Fatih Bulut[3], Asli Garagon[3], Yuri Fialko[1]

Affiliations:
[1] Scripps Institution of Oceanography, UC San Diego; La Jolla, CA 92093, USA
[2] Department of Earth and Environmental Sciences, Ludwig-Maximilians-Universität München; Munich, 80539, Germany
[3] Geodesy Department, Bogazici University Kandilli Observatory and Earthquake Research Institute; Istanbul, 34342, Turkey
[*] Corresponding author. Email: z5jia@ucsd.edu

Abstract: The destructive 2023 moment magnitude (M_w) 7.8-7.7 earthquake doublet ruptured multiple segments of the East Anatolian Fault system in Turkey. We integrate multi-scale seismic and space-geodetic observations with multi-fault kinematic inversions and dynamic rupture modeling to unravel the events' complex rupture history and stress-mediated fault interactions. Our analysis reveals three sub-shear slip episodes during the initial M_w 7.8 earthquake with delayed rupture initiation to the southwest. The M_w 7.7 event occurred 9 hours later with larger slip and supershear rupture on its western branch. Mechanically consistent dynamic models accounting for fault interactions can explain the unexpected rupture paths, and require a heterogeneous background stress. Our results highlight the importance of combining near- and far-field observations with data-driven and physics-based models for seismic hazard assessment.

One-Sentence Summary: Seismic and geodetic imaging and dynamic rupture modeling unravel dynamics and interactions of the Turkey earthquake doublet.

Main Text:

Introduction

The moment magnitude (M_w) 7.8 and 7.7 Kahramanmaraş earthquakes in Turkey on February 6, 2023, caused enormous destruction and tens of thousands of casualties from collapsed structures, and were one of the deadliest natural disasters for Turkey and Syria over the last millennium (*1*). The Kahramanmaraş sequence is the first great earthquake doublet with a combined moment magnitude of 8 recorded in a continental strike-slip fault system. Unlike regular aftershocks that are over one order of magnitude smaller than their mainshock, doublet events pose a greater hazard as they can cause more severe damage by striking already weakened buildings and structures. We show that the Kahramanmaraş earthquake doublet involved a remarkable sequence of sub-events that occurred with varying rupture velocities, geometries, and time delays on branched fault segments, which challenge our understanding of earthquake interactions and the dynamics of rupture propagation.

Seismologists commonly approximate earthquakes as point sources or as slip along a single fault with fixed rupture velocity. However, large earthquakes often rupture multiple fault segments within a complex network (*2*-*6*). Occasionally, events of a comparable magnitude occur within minutes to hours of the initial event, resulting in earthquake doublets (*7*-*9*). Branching faults may further complicate rupture dynamics (*10*-*12*). Whether rupture stops or continues propagating at fault junctions can determine earthquakes' eventual size and destructive potential (*13*). When applied to complex ruptures on multiple faults, conventional earthquake source imaging often involves oversimplified assumptions, yielding stark differences in source models and their interpretations (*14, 15*). Initial studies of the Kahramanmaraş earthquakes presented a wide range of earthquake models and interpretations (*16*-*21*), likely due to focusing on particular datasets and aspects of the rupture process. These differences motivate unified and self-consistent approaches that integrate diverse datasets with state-of-the-art rupture models to advance our understanding of the earthquake dynamics.

We perform a comprehensive investigation of the M_w 7.8-7.7 Kahramanmaraş doublet using data-driven and physics-based analyses applied to near- and far-field seismic and geodetic observations. Our results reveal that the earthquakes followed unexpected rupture trajectories, which included delayed backward branching, statically- and dynamically aided triggering, and a combination of subshear and supershear rupture episodes. These discoveries call for reevaluating the role of cascading failure mechanisms when assessing the destructive potential of large earthquakes within complex fault networks.

The geometrically complex M_w 7.8-7.7 earthquake doublet

On Feb 6, 2023, two major (moment magnitude greater than 7) earthquakes ruptured several previously recognized fault systems within nine hours (Fig. 1). The EAF is a mature transform fault accommodating up to 10 mm/y of left-lateral motion between the Arabian and Anatolian plates (*22*) (Fig. 1). Several M_w ~7 earthquakes occurred on the EAF historically, but none ruptured the entire southern section of the EAF (*23*). The estimated dimensions of the historic events suggest that geometric complexities such as fault bends and step-overs may have controlled the event sizes (*23, 24*). The second earthquake (M_w 7.7) occurred on the Savrun-Çardak Fault (SCF), extending ~150 km along the east-west direction (Fig. 1). The SCF has been relatively quiescent, with only two moderate (M_w <6) events recorded in the past 100 years (*25*).

We constrain the rupture geometry based on surface traces mapped using Synthetic Aperture Radar data (*26*) and precisely relocated aftershocks (*27, 28*). We find that the Kahramanmaraş doublet ruptured at least six major fault segments (Fig. 1). The epicenter of the M_w 7.8 earthquake is located on a subsidiary fault, the Nurdağı-Pazarcık Fault (NPF, fault 1 in Fig. 1A) (*20*), from which the rupture propagated to the EAF, and then ruptured along the EAF to both the northeast and southwest (faults 2 and 3), for a total length of about 300 km. Unlike the historical M~7 events, the M_w 7.8 earthquake propagated across at least four possible geometric barriers, including fault bends and stepovers.

The static slip distribution (Fig. 1B) obtained from inversions of Synthetic Aperture Radar (SAR) and Global Navigation Satellite System (GNSS) data (Fig. S1-S7) shows that the largest slip in the M_w 7.8 event is on the EAF at its junction with the NPF, near the towns of Kahramanmaraş and Pazarcık, with peak slip in excess of 8 m. Most of the coseismic slip is in the upper 20 km of the seismogenic layer (Fig. 1B). Slip at the surface is highly heterogeneous, consistent with field observations (*18*), but on average increasing from the southwest to the northeast ends of the M_w 7.8 rupture (Fig. S8). The area of substantial slip extends to the northeast from the junction for about 150 km to the western tip of the 2020 M_w 6.7 Elazig rupture (*29*) (Fig. 1A). South of the junction, the M_w 7.8 rupture extends to the southern end of the EAF. The average coseismic slip on the southwest branch of the M_w 7.8 rupture is smaller than the average slip on the northeast branch (Figs. 1B and S2).

We resolve the spatiotemporal rupture process with a subevent inversion method using both near- and far-field seismic observations (*30, 31*). The M_w 7.8 earthquake has six subevents altogether spanning ~90 s (Fig. 2A). The M_w 6.8 subevent E1 that ruptures the NPF is followed 18 s later by the largest subevent E2 (M_w 7.5) at the NPF-EAF intersection. The earthquake then ruptured northeastward along the EAF for about 130 km (M_w 7.5 subevent E3), as well as, after a short delay, backward from the NPF junction for about 150 km along the southwestern segment of the EAF, with integrated slip equivalent to a M_w 7.4 earthquake (subevents E4-E6). Teleseismic P-wave back-projection (*32*) confirms the rupture process with imaged high-frequency radiation peaks outlining the major subevents (Fig. 2A) and indicating an average rupture velocity of 3 km/s. To further constrain the slip history, we perform a joint kinematic slip inversion of the M_w 7.8 earthquake constrained by far- and near-field seismic and geodetic data (*26, 33*). Our kinematic inversion results agree with the static and subevent models (Fig. 2B). The best-fit kinematic slip model images 10-s-delayed backward branching at the NPF-EAF intersection, toward the southwest (Fig. 2B), constrained by the strong-motion data (Fig. S17). It also indicates average rupture velocities of 3.2 km/s and 2.8 km/s for the northeastern and southwestern branches, respectively (Fig. S18). Tracking ground motion pulses at near-fault strong motion stations along the southwestern segment, also yields a rupture velocity of ~3 km/s (Fig. S18), confirming an overall subshear nature. All our kinematic models consistently reveal a ~300 km-long complex bilateral multi-segment rupture, subshear rupture velocities, and delayed triggering of the southwest segment of the M_w 7.8 event (Fig. 2C).

The subsequent M_w 7.7 earthquake ruptured a 150-km long section of the west-trending SCF, within 90 km of the M_w 7.8 earthquake hypocenter. The aftershock distribution and surface offsets indicate branching and abrupt changes in strike at both the eastern and western ends of the M_w 7.7 rupture (Fig. 1). Geodetic data and our associated static slip model (Fig. 1B) suggest rupture along an 80-km-long segment of the SCF system (fault 4-5 in Fig. 1), but not along the eastern end of the Sürgü fault that connects to the EAF. Instead, the M_w 7.7 rupture diverted sharply onto the Doğanşehir branch, which angles to the northeast (fault 6). The M_w 7.7 event shows a concentrated slip distribution with over 10 m peak slip around its hypocenter, suggesting a substantially higher stress drop than the initial M_w 7.8 earthquake which spreads lower-amplitude slip over a larger region.

Our analysis of the rupture history of the M_w 7.7 event identifies four major subevents, lasting for about 30 seconds (Fig. 3A). The first three subevents, E1-E3, all cluster near the epicenter and account for over 80% of the total seismic moment, suggesting a compact bilateral rupture in the central SCF. The focal mechanism (strike of 237°) and location of the last subevent (E4, M_w 7.1) agree with the static slip model on the Doğanşehir branch (Fig. 1B). All subevents of both earthquakes have almost pure double-couple mechanisms (Figs. 2A and 3A), suggesting that the strong non-double couple components in the Global Centroid-Moment-Tensor solutions (*34*) (Fig. 1A) are due to highly variable rupture geometries. The overall shorter duration and smaller rupture extent of the M_w 7.7 event make back-projection analysis less effective for resolving rupture details, but our kinematic finite-slip inversion can still be applied.

The kinematic finite-fault model of the M_w 7.7 earthquake also indicates a compact slip distribution. In addition, it indicates a westward rupture velocity of approximately 4.5 km/s (Fig. 3B), exceeding the shear-wave speed in the crust. The waveforms recorded at the westward seismic stations strongly constrain this supershear rupture episode (Fig 3C, Fig. S19), which is consistent with analysis of high-rate GNSS data (*20*). In contrast, the eastward rupture likely propagated at a slower velocity of 2.5 km/s. The intriguing supershear rupture episode may imply locally higher prestress (*35*) and high stress drop (*36*) as in our dynamic rupture models.

Dynamics, triggering, and stress interaction of the doublet

Dynamic rupture modeling involves simulating how earthquakes nucleate, propagate, and arrest. Unlike purely data-driven kinematic slip inversions, such models predict the evolution of slip, seismic waves, and surface deformation in a physically self-consistent manner. Detailed, physics-based interpretations can help verify whether inferred rupture scenarios are mechanically plausible, but are computationally challenging and typically take years to develop (e.g., *10*,*12*,*13*).

We present data-informed dynamic rupture simulations of the 2023 Kahramanmaraş earthquakes that illuminate complex details of the rupture process. Our 3D dynamic rupture models include stress changes computed from the slip distribution of the static slip model (*37*), large-scale variability in fault loading inferred from regional seismo-tectonics, and the relative effects of the static and dynamic stresses of the M_w 7.8 event on the faults hosting the second earthquake (*26*, Fig. S20). The dynamic rupture models independently reproduce the main features of the kinematic models (Fig. 4, Fig. S21), providing a physics-based validation of the inferred rupture histories.

Our forward simulations use the complex fault geometries of both earthquakes informed from geodetic analysis (Fig. 1) to spontaneously replicate the moment rate release, magnitude, rupture velocity and delays, as well as the lack of instantaneous dynamic triggering of the M_w 7.7 event. The dynamic rupture synthetics produce surface displacements and slip histories that compare well to the high-resolution geodetic data (Fig. S22), kinematic rupture representations (Figs. 4, S21) and observed ground motions (Figs. 5, S23-25). Figure 4A illustrates the modeled M_w 7.8 earthquake dynamics. The NPF-EAF intersection slows sub-shear rupture on the NPF which then branches with dynamically favorable forward directivity (*38*) northeastward along the EAF. The large fault branching angle poses a strong dynamic barrier in backward-directivity (*39*) leading to significantly delayed EAF rupture toward the southwest. Continuous dynamic unclamping, transient shear stressing and static stress build-up at the fault intersection due to the unilaterally propagating northeast rupture allows the rupture to eventually fracture the EAF bilaterally (Fig. S26). Rupture speed remains overall sub-shear during the earthquake (Fig. 4B).

Dynamic rupture modeling of the M_w 7.7 earthquake features bi-lateral rupture with unequal rupture speeds, confirming dominant supershear westward and sub-shear eastward propagation. Our M_w 7.8 dynamic rupture model predicts a highly variable pattern of static and dynamic stresses resolved on the faults that hosted the M_w 7.7 earthquake (Figs. 4C, D). The hypocentral area of the M_w 7.7 event experienced an increase in static Coulomb stress of several hundred kilopascals due to the M_w 7.8 earthquake, resulting from both an increase in shear stress and a decrease in fault-normal compression (Fig. S27). It also experienced a much larger transient increase in the Coulomb stress of a few megapascals due to passing seismic waves (Fig. 4D), which nevertheless did not result in instantaneous triggering.

Discussion and Conclusions

Our analyses reveal unexpected rupture paths. The Kahramanmaraş doublet originated as a moderate event on the NPF branch fault with a magnitude of only 6.8, yet the rupture was able to successfully cross the junction of the NPF and EAF, which would usually be considered a geometric barrier that conditionally gates the rupture propagation (*40, 41*). As a result, the earthquake intensified with the northeastward propagation along the EAF, then dynamically triggered backward rupture toward the southwest by continuously unclamping and stressing from the forward branch, eventually culminating in a M_w 7.8 event, with total seismic moment increased by a factor of 30 compared to the initial rupture on the NPF. In addition, the M_w 7.8 earthquake increased the Coulomb stress on the central part of the SCF, which may have aided the nucleation of the M_w 7.7 earthquake 9 hours later. The entire process highlights the additional hazard brought by rupture triggering across a network of faults, challenging earthquake hazard assessments that typically do not consider such multi-fault triggering scenarios.

The M_w 7.8 earthquake involved backward fault branching, which is highly unfavorable from a dynamic perspective, thus commonly neglected in hazard studies. Several previous continental earthquakes, including the 1992 Landers, the 1999 Hector Mine, and the 2002 Denali earthquakes, have also exhibited localized backward branching (*10*). Existing explanations of this phenomenon include backward rupture jumping induced by sudden rupture arresting or nonuniform prestress fields caused by earthquake cycles (*39, 42*). Our dynamic rupture models indicate that backward branching during the M_w 7.8 event does not necessarily require a complex arrangement of the receiver fault (*42*) or triggering of supershear rupture (*43*). Instead, the progressive build-up of slip on the forward branch of the EAF continuously unclamps and stresses the backward branch of the EAF, eventually leading to delayed and self-sustained branching towards the southwest, which is a simple yet effective mechanism.

One of the surprising aspects of the M_w 7.7 earthquake is that it did not rupture through the eastern Sürgü segment and arrive at the EAF, contrary to earlier suggestions (*20*), but instead deviated to the Doğanşehir branch. The InSAR, aftershock, and seismic data clearly show such a deviation (Fig. S1, S14). The straightforward rupture path along the Sürgü fault was encouraged by the static stress changes due to the M_w 7.8 event (Fig. S27), unlike the sharp deviation to the

Doğanşehir fault which was actually unloaded by the M_w 7.8 event (Fig. 4D and Video S3). Possible explanations, which may be tested by future geodetic and seismological observations, include velocity-strengthening behavior of the eastern Sürgü segment, or local stress heterogeneity, e.g., due to past earthquakes (*44*). Considerable regional stress heterogeneity, as is required by our dynamic rupture models (Fig. S20), is implied by extremely complex rupture geometries involving changes in the strike angle of up to 90 degrees (Fig. 1, Fig. S27) (*45*). Some faults in the study area, including the EAF, exhibit shallow creep (*46*), however creep has to be pervasive to potentially suppress an incoming dynamic rupture. Observations spanning all phases of the earthquake cycle are needed to constrain the velocity- and depth-dependent frictional properties of active faults (*47, 48*). Shallow creep might be responsible for a substantial reduction in the amplitude of coseismic slip in the top few kilometers of the upper crust (Fig. 1B), which is well resolved in our inverse models (Fig. S28). Subsequent observations will show whether this reduction can be compensated by shallow afterslip or constitutes a long-term shallow slip deficit (*49*), implying wide-spread off-fault yielding (*47, 50*).

We also find intriguing variations in rupture velocity across segments of the EAF-SCF fault network. Although the M_w 7.8 event produced extreme shaking with peak ground accelerations (PGA) exceeding 1g for near-fault stations, the observed and simulated M_w 7.7 ground motions are similar or larger when compared at the same distance (Fig. 5, Fig. S23-S24), consistent with a potentially larger stress drop of the M_w 7.7 event. The modeled and observed M_w 7.7 event shaking shows less distance dependence, which may be due to the effects of supershear rupture.

The western branch of the SCF experienced a supershear rupture episode, while the eastern SCF branch and the EAF hosted subshear ruptures with considerable delays. In general, our modeling shows that the pre-event stress heterogeneities, dynamic and static redistribution of stress and the geometry of the faults may control these diverse rupture characteristics.

The Kahramanmaraş doublet ruptured multiple faults in distinct slip episodes, likely involving complex stress-triggering processes across different temporal and spatial scales. Such processes resulted in the increased rupture length and seismic moment of the Turkey earthquake doublet, and a substantially larger destructive potential compared with the "typical" M_w ~7 historical earthquakes in the region (*23*). Such a variability might be interpreted in terms of the super-cycle model (*51*). By using integrated methods that combine near- and far-field seismic and geodetic observations and investigating data-derived models and physics-based rupture simulations, we show that stress interactions, and static and dynamic triggering worked together across a complex fault system, resulting in a cascade of rupture with a larger than usual total rupture length and moment magnitude. Our study shows that complementary data-driven and physics-based analyses, which in isolation often lead to non-unique or even contradictory results, can jointly and efficiently unravel highly complex earthquake dynamics based on dense near-field observations. The unusual static and dynamic interactions during and between the events of the Kahramanmaraş doublet call for reassessment of common assumptions built into seismic hazard assessments.

References and Notes

1. M. Edrik, M. B. D. Tümsa, A. Pınar, E. Altunel, A. C. Zülfikar, "A preliminary report on the February 6, 2023 earthquakes in Türkiye" (*temblor*, 2023);

2. T. Lay, L. Ye, Y. Bai, K. F. Cheung, H. Kanamori, The 2018 MW 7.9 Gulf of Alaska earthquake: Multiple fault rupture in the Pacific plate. *Geophysical Research Letters* **45**, 9542-9551 (2018).
3. L. Meng, J.-P. Ampuero, J. Stock, Z. Duputel, Y. Luo, V. Tsai, Earthquake in a maze: Compressional rupture branching during the 2012 M w 8.6 Sumatra earthquake. *Science* **337**, 724-726 (2012).
4. E. Hauksson, L. M. Jones, K. Hutton, The 1999 M w 7.1 Hector Mine, California, earthquake sequence: complex conjugate strike-slip faulting. *Bulletin of the Seismological Society of America* **92**, 1154-1170 (2002).
5. E. Hauksson, L. M. Jones, K. Hutton, D. Eberhart-Phillips, The 1992 Landers earthquake sequence: Seismological observations. *Journal of Geophysical Research: Solid Earth* **98**, 19835-19858 (1993).
6. Z. E. Ross, B. Idini, Z. Jia, O. L. Stephenson, M. Zhong, X. Wang, Z. Zhan, M. Simons, E. J. Fielding, S.-H. Yun, Hierarchical interlocked orthogonal faulting in the 2019 Ridgecrest earthquake sequence. *Science* **366**, 346-351 (2019).
7. A. Ghods, E. Shabanian, E. Bergman, M. Faridi, S. Donner, G. Mortezanejad, A. Aziz-Zanjani, The Varzaghan–Ahar, Iran, Earthquake Doublet (M w 6.4, 6.2): implications for the geodynamics of northwest Iran. *Geophysical Journal International* **203**, 522-540 (2015).
8. C. J. Ammon, H. Kanamori, T. Lay, A great earthquake doublet and seismic stress transfer cycle in the central Kuril islands. *Nature* **451**, 561-565 (2008).
9. W. Fan, P. M. Shearer, Local near instantaneously dynamically triggered aftershocks of large earthquakes. *Science* **353**, 1133-1136 (2016).
10. D. D. Oglesby, S. M. Day, Y.-G. Li, J. E. Vidale, The 1999 Hector Mine earthquake: The dynamics of a branched fault system. *Bulletin of the Seismological Society of America* **93**, 2459-2476 (2003).
11. H. S. Bhat, M. Olives, R. Dmowska, J. R. Rice, Role of fault branches in earthquake rupture dynamics. *Journal of Geophysical Research: Solid Earth* **112**, (2007).
12. T. Ulrich, A.-A. Gabriel, J.-P. Ampuero, W. Xu, Dynamic viability of the 2016 Mw 7.8 Kaikōura earthquake cascade on weak crustal faults. *Nature communications* **10**, 1213 (2019).
13. R. Douilly, H. Aochi, E. Calais, A. Freed, Three-dimensional dynamic rupture simulations across interacting faults: The Mw7. 0, 2010, Haiti earthquake. *Journal of Geophysical Research: Solid Earth* **120**, 1108-1128 (2015).
14. S. Minson, M. Simons, J. Beck, Bayesian inversion for finite fault earthquake source models I—Theory and algorithm. *Geophysical Journal International* **194**, 1701-1726 (2013).
15. K. Wang, D. S. Dreger, E. Tinti, R. Bürgmann, T. a. Taira, Rupture process of the 2019 Ridgecrest, California M w 6.4 foreshock and M w 7.1 earthquake constrained by seismic and geodetic data. *Bulletin of the Seismological Society of America* **110**, 1603-1626 (2020).
16. S. Barbot, H. Luo, T. Wang, Y. Hamiel, O. Piatibratova, M. T. Javed, C. Braitenberg, G. Gurbuz, Slip distribution of the February 6, 2023 Mw 7.8 and Mw 7.6, Kahramanmaraş, Turkey earthquake sequence in the East Anatolian Fault Zone. *Seismica* **2**, (2023).
17. D. E. Goldberg, T. Taymaz, N. G. Reitman, A. E. Hatem, S. Yolsal-Çevikbilen, W. D. Barnhart, T. S. Irmak, D. J. Wald, T. Öcalan, W. L. Yeck, Rapid Characterization of the

February 2023 Kahramanmaraş, Türkiye, Earthquake Sequence. *The Seismic Record* **3**, 156-167 (2023).

18. V. Karabacak, Ç. Özkaymak, H. Sözbilir, O. Tatar, B. Aktuğ, Ö. C. Özdağ, R. Çakir, E. Aksoy, F. Koçbulut, M. Softa. (The Geological Society of London, 2023), vol. 180, pp. jgs2023-2020.
19. P. M. Mai, T. Aspiotis, T. A. Aquib, E. V. Cano, D. Castro-Cruz, A. Espindola-Carmona, B. Li, X. Li, J. Liu, R. Matrau, The Destructive Earthquake Doublet of 6 February 2023 in South-Central Türkiye and Northwestern Syria: Initial Observations and Analyses. *The Seismic Record* **3**, 105-115 (2023).
20. D. Melgar, T. Taymaz, A. Ganas, B. Crowell, T. Öcalan, M. Kahraman, V. Tsironi, S. Yolsal-Çevikbilen, S. Valkaniotis, T. S. Irmak, T. Eken, C. Erman, B. Özkan, A. H. Dogan, C. Altuntaş, Sub- and super-shear ruptures during the 2023 Mw 7.8 and Mw 7.6 earthquake doublet in SE Türkiye. *Seismica* **2**, (2023).
21. R. Okuwaki, Y. Yagi, T. Taymaz, S. P. Hicks, Multi-Scale Rupture Growth With Alternating Directions in a Complex Fault Network During the 2023 South-Eastern Türkiye and Syria Earthquake Doublet. *Geophysical Research Letters* **50**, e2023GL103480 (2023).
22. N. Lyberis, T. Yurur, J. Chorowicz, E. Kasapoglu, N. Gundogdu, The East Anatolian Fault: an oblique collisional belt. *Tectonophysics* **204**, 1-15 (1992).
23. S. E. Güvercin, H. Karabulut, A. Ö. Konca, U. Doğan, S. Ergintav, Active seismotectonics of the East Anatolian Fault. *Geophysical Journal International* **230**, 50-69 (2022).
24. T. Y. Duman, Ö. Emre, The East Anatolian Fault: geometry, segmentation and jog characteristics. *Geological Society, London, Special Publications* **372**, 495-529 (2013).
25. A. Koc, N. Kaymakcı, Kinematics of Sürgü fault zone (Malatya, Turkey): A remote sensing study. *Journal of Geodynamics* **65**, 292-307 (2013).
26. Materials and methods are available as supplementary materials.
27. Z. Jin, Y. Fialko, Finite slip models of the 2019 Ridgecrest earthquake sequence constrained by space geodetic data and aftershock locations. *Bulletin of the Seismological Society of America* **110**, 1660-1679 (2020).
28. A. Lomax, Precise, NLL-SSST-coherence hypocenter catalog for the 2023 M_w 7.8 and M_w 7.6 SE Turkey earthquake sequence, Zenodo (2023); https://10.5281/zenodo.7699881
29. A. Doğru, F. Bulut, C. Yaltırak, B. Aktuğ, Slip distribution of the 2020 Elazığ Earthquake (M w 6.75) and its influence on earthquake hazard in the Eastern Anatolia. *Geophysical Journal International* **224**, 389-400 (2021).
30. Z. Jia, Z. Shen, Z. Zhan, C. Li, Z. Peng, M. Gurnis, The 2018 Fiji Mw 8.2 and 7.9 deep earthquakes: One doublet in two slabs. *Earth and Planetary Science Letters* **531**, 115997 (2020).
31. Z. Jia, Z. Zhan, H. Kanamori, The 2021 south Sandwich Island Mw 8.2 Earthquake: A slow event sandwiched between regular ruptures. *Geophysical Research Letters* **49**, e2021GL097104 (2022).
32. M. Ishii, P. M. Shearer, H. Houston, J. E. Vidale, Extent, duration and speed of the 2004 Sumatra–Andaman earthquake imaged by the Hi-Net array. *Nature* **435**, 933-936 (2005).

33. Z. Jia, X. Wang, Z. Zhan, Multifault models of the 2019 Ridgecrest sequence highlight complementary slip and fault junction instability. *Geophysical Research Letters* **47**, e2020GL089802 (2020).
34. G. Ekström, M. Nettles, A. Dziewoński, The global CMT project 2004–2010: Centroid-moment tensors for 13,017 earthquakes. *Physics of the Earth and Planetary Interiors* **200**, 1-9 (2012).
35. C. Liang, J. P. Ampuero, D. Pino Muñoz, The paucity of supershear earthquakes on large faults governed by rate and state friction. *Geophysical Research Letters* **49**, e2022GL099749 (2022).
36. E. M. Dunham, Conditions governing the occurrence of supershear ruptures under slip-weakening friction. *Journal of Geophysical Research: Solid Earth* **112**, (2007).
37. E. Tinti, E. Casarotti, T. Ulrich, T. Taufiqurrahman, D. Li, A.-A. Gabriel, Constraining families of dynamic models using geological, geodetic and strong ground motion data: The Mw 6.5, October 30th, 2016, Norcia earthquake, Italy. *Earth and Planetary Science Letters* **576**, 117237 (2021).
38. N. Kame, J. R. Rice, R. Dmowska, Effects of prestress state and rupture velocity on dynamic fault branching. *Journal of Geophysical Research: Solid Earth* **108**, (2003).
39. S. Fliss, H. S. Bhat, R. Dmowska, J. R. Rice, Fault branching and rupture directivity. *Journal of Geophysical Research: Solid Earth* **110**, (2005).
40. G. King, J. Nábělek, Role of fault bends in the initiation and termination of earthquake rupture. *Science* **228**, 984-987 (1985).
41. D. Andrews, Mechanics of fault junctions. *Journal of Geophysical Research: Solid Earth* **94**, 9389-9397 (1989).
42. B. Duan, D. D. Oglesby, Nonuniform prestress from prior earthquakes and the effect on dynamics of branched fault systems. *Journal of Geophysical Research: Solid Earth* **112**, (2007).
43. A. Rosakis, M. Abdelmeguid, A. Elbanna, Evidence of Early Supershear Transition in the M_w 7.8 Kahramanmaraş Earthquake From Near-Field Records. *arXiv:2302.07214*, (2023).
44. S. S. Nalbant, J. McCloskey, S. Steacy, A. A. Barka, Stress accumulation and increased seismic risk in eastern Turkey. *Earth and Planetary Science Letters* **195**, 291-298 (2002).
45. Y. Fialko, Estimation of absolute stress in the hypocentral region of the 2019 Ridgecrest, California, earthquakes. *Journal of Geophysical Research: Solid Earth* **126**, e2021JB022000 (2021).
46. Z. Cakir, U. Doğan, A. M. Akoğlu, S. Ergintav, S. Özarpacı, A. Özdemir, T. Nozadkhalil, N. Çakir, C. Zabcı, M. H. Erkoç, Arrest of the Mw 6.8 January 24, 2020 Elaziğ (Turkey) earthquake by shallow fault creep. *Earth and Planetary Science Letters* **608**, 118085 (2023).
47. Y. Kaneko, Y. Fialko, D. T. Sandwell, X. Tong, M. Furuya, Interseismic deformation and creep along the central section of the North Anatolian Fault (Turkey): InSAR observations and implications for rate-and-state friction properties. *Journal of Geophysical Research: Solid Earth* **118**, 316-331 (2013).
48. E. O. Lindsey, Y. Fialko, Geodetic constraints on frictional properties and earthquake hazard in the Imperial Valley, Southern California. *Journal of Geophysical Research: Solid Earth* **121**, 1097-1113 (2016).

49. Y. Fialko, D. Sandwell, M. Simons, P. Rosen, Three-dimensional deformation caused by the Bam, Iran, earthquake and the origin of shallow slip deficit. *Nature* **435**, 295-299 (2005).
50. Z. Jin, Y. Fialko, Coseismic and early postseismic deformation due to the 2021 M7. 4 Maduo (China) earthquake. *Geophysical Research Letters* **48**, e2021GL095213 (2021).
51. L. Dal Zilio, J.-P. Ampuero, Earthquake doublet in Turkey and Syria. *Communications Earth & Environment* **4**, 71 (2023).
52. L. Luzi, F. Pacor, G. Lanzano, C. Felicetta, R. Puglia, M. D'Amico, 2016–2017 Central Italy seismic sequence: strong-motion data analysis and design earthquake selection for seismic microzonation purposes. *Bulletin of Earthquake Engineering* **18**, 5533-5551 (2020).
53. Disaster and Emergency Management Authority (AFAD), (1973); https://deprem.afad.gov.tr/event-catalog
54. T. Taufiqurrahman, A.-A. Gabriel, D. Li, T. Ulrich, B. Li, S. Carena, A. Verdecchia, F. Gallovič, Dynamics, interactions and delays of the 2019 Ridgecrest rupture sequence. *Nature*, 1-8 (2023).
55. S. Akkar, M. A. Sandıkkaya, J. J. Bommer, Empirical ground-motion models for point- and extended-source crustal earthquake scenarios in Europe and the Middle East. *Bulletin of earthquake engineering* **12**, 359-387 (2014).
56. D. Sandwell, R. Mellors, X. Tong, M. Wei, P. Wessel, GMTSAR: An InSAR processing system based on generic mapping tools. (2011).
57. T. G. Farr, P. A. Rosen, E. Caro, R. Crippen, R. Duren, S. Hensley, M. Kobrick, M. Paller, E. Rodriguez, L. Roth, The shuttle radar topography mission. *Reviews of geophysics* **45**, (2007).
58. R. M. Goldstein, H. A. Zebker, C. L. Werner, Satellite radar interferometry: Two-dimensional phase unwrapping. *Radio science* **23**, 713-720 (1988).
59. T. A. Herring, T. I. Melbourne, M. H. Murray, M. A. Floyd, W. M. Szeliga, R. W. King, D. A. Phillips, C. M. Puskas, M. Santillan, L. Wang, Plate Boundary Observatory and related networks: GPS data analysis methods and geodetic products. *Reviews of Geophysics* **54**, 759-808 (2016).
60. J. Böhm, A. Niell, P. Tregoning, H. Schuh, Global Mapping Function (GMF): A new empirical mapping function based on numerical weather model data. *Geophysical research letters* **33**, (2006).
61. F. Lyard, F. Lefevre, T. Letellier, O. Francis, Modelling the global ocean tides: modern insights from FES2004. *Ocean dynamics* **56**, 394-415 (2006).
62. D. D. McCarthy, G. Petit, "IERS conventions (2003)" (International Earth Rotation And Reference Systems Service (Iers)(Germany), 2004).
63. K. Wang, Y. Fialko, Slip model of the 2015 Mw 7.8 Gorkha (Nepal) earthquake from inversions of ALOS-2 and GPS data. *Geophysical Research Letters* **42**, 7452-7458 (2015).
64. Y. Fialko, Probing the mechanical properties of seismically active crust with space geodesy: Study of the coseismic deformation due to the 1992 Mw7. 3 Landers (southern California) earthquake. *Journal of Geophysical Research: Solid Earth* **109**, (2004).
65. R. Wang, F. L. Martín, F. Roth, Computation of deformation induced by earthquakes in a multi-layered elastic crust—FORTRAN programs EDGRN/EDCMP. *Computers & Geosciences* **29**, 195-207 (2003).

66. T. Bodin, M. Sambridge, H. Tkalčić, P. Arroucau, K. Gallagher, N. Rawlinson, Transdimensional inversion of receiver functions and surface wave dispersion. *Journal of geophysical research: solid earth* **117**, (2012).
67. S. E. Minson, D. S. Dreger, Stable inversions for complete moment tensors. *Geophysical Journal International* **174**, 585-592 (2008).
68. B. Kennett, E. Engdahl, Traveltimes for global earthquake location and phase identification. *Geophysical Journal International* **105**, 429-465 (1991).
69. M. Kikuchi, H. Kanamori, Inversion of complex body waves—III. *Bulletin of the Seismological Society of America* **81**, 2335-2350 (1991).
70. Y. Qian, S. Ni, S. Wei, R. Almeida, H. Zhang, The effects of core-reflected waves on finite fault inversions with teleseismic body wave data. *Geophysical Journal International* **211**, 936-951 (2017).
71. L. Zhu, L. A. Rivera, A note on the dynamic and static displacements from a point source in multilayered media. *Geophysical Journal International* **148**, 619-627 (2002).
72. W. Fan, P. M. Shearer, Detailed rupture imaging of the 25 April 2015 Nepal earthquake using teleseismic P waves. *Geophysical Research Letters* **42**, 5744-5752 (2015).
73. E. Nissen, J. Elliott, R. Sloan, T. Craig, G. Funning, A. Hutko, B. Parsons, T. Wright, Limitations of rupture forecasting exposed by instantaneously triggered earthquake doublet. *Nature Geoscience* **9**, 330-336 (2016).
74. D. Wang, N. Takeuchi, H. Kawakatsu, J. Mori, Estimating high frequency energy radiation of large earthquakes by image deconvolution back-projection. *Earth and Planetary Science Letters* **449**, 155-163 (2016).
75. S. P. Hicks, R. Okuwaki, A. Steinberg, C. A. Rychert, N. Harmon, R. E. Abercrombie, P. Bogiatzis, D. Schlaphorst, J. Zahradnik, J.-M. Kendall, Back-propagating supershear rupture in the 2016 M w 7.1 Romanche transform fault earthquake. *Nature Geoscience* **13**, 647-653 (2020).
76. S. Rost, C. Thomas, Array seismology: Methods and applications. *Reviews of geophysics* **40**, 2-1-2-27 (2002).
77. Y. Xu, K. D. Koper, O. Sufri, L. Zhu, A. R. Hutko, Rupture imaging of the Mw 7.9 12 May 2008 Wenchuan earthquake from back projection of teleseismic P waves. *Geochemistry, Geophysics, Geosystems* **10**, (2009).
78. S. H. Hartzell, T. H. Heaton, Rupture history of the 1984 Morgan Hill, California, earthquake from the inversion of strong motion records. *Bulletin of the Seismological Society of America* **76**, 649-674 (1986).
79. C. Ji, D. J. Wald, D. V. Helmberger, Source description of the 1999 Hector Mine, California, earthquake, part I: Wavelet domain inversion theory and resolution analysis. *Bulletin of the Seismological Society of America* **92**, 1192-1207 (2002).
80. M. Grant, S. Boyd, CVX: Matlab software for disciplined convex programming, version 2.1, (2014).
81. R. A. Harris, M. Barall, D. J. Andrews, B. Duan, S. Ma, E. M. Dunham, A.-A. Gabriel, Y. Kaneko, Y. Kase, B. T. Aagaard, Verifying a computational method for predicting extreme ground motion. *Seismological Research Letters* **82**, 638-644 (2011).
82. M. D. Ramos, P. Thakur, Y. Huang, R. A. Harris, K. J. Ryan, Working with dynamic earthquake rupture models: A practical guide. *Seismological Society of America* **93**, 2096-2110 (2022).

83. D. Andrews, Rupture propagation with finite stress in antiplane strain. *Journal of Geophysical Research* **81**, 3575-3582 (1976).
84. S. Das, K. Aki, Fault plane with barriers: A versatile earthquake model. *Journal of geophysical research* **82**, 5658-5670 (1977).
85. E. H. Madden, T. Ulrich, A. A. Gabriel, The State of Pore Fluid Pressure and 3-D Megathrust Earthquake Dynamics. *Journal of Geophysical Research: Solid Earth* **127**, e2021JB023382 (2022).
86. J. R. Rice, "Fault stress states, pore pressure distributions, and the weakness of the San Andreas fault" in *International geophysics* (Elsevier, 1992), vol. 51, pp. 475-503.
87. J. Suppe, Fluid overpressures and strength of the sedimentary upper crust. *Journal of Structural Geology* **69**, 481-492 (2014).
88. S. Wollherr, A. A. Gabriel, P. M. Mai, Landers 1992 “reloaded”: Integrative dynamic earthquake rupture modeling. *Journal of Geophysical Research: Solid Earth* **124**, 6666-6702 (2019).
89. T. Ulrich, A.-A. Gabriel, E. H. Madden, Stress, rigidity and sediment strength control megathrust earthquake and tsunami dynamics. *Nature Geoscience* **15**, 67-73 (2022).
90. J. R. Weiss, R. J. Walters, Y. Morishita, T. J. Wright, M. Lazecky, H. Wang, E. Hussain, A. J. Hooper, J. R. Elliott, C. Rollins, High-resolution surface velocities and strain for Anatolia from Sentinel-1 InSAR and GNSS data. *Geophysical Research Letters* **47**, e2020GL087376 (2020).
91. S. Peyrat, K. Olsen, Nonlinear dynamic rupture inversion of the 2000 Western Tottori, Japan, earthquake. *Geophysical research letters* **31**, (2004).
92. F. Gallovič, Ľ. Valentová, J. P. Ampuero, A. A. Gabriel, Bayesian dynamic finite-fault inversion: 1. Method and synthetic test. *Journal of Geophysical Research: Solid Earth* **124**, 6949-6969 (2019).
93. E. Tinti, P. Spudich, M. Cocco, Earthquake fracture energy inferred from kinematic rupture models on extended faults. *Journal of Geophysical Research: Solid Earth* **110**, (2005).
94. H. Weng, H. Yang, Constraining frictional properties on fault by dynamic rupture simulations and near-field observations. *Journal of Geophysical Research: Solid Earth* **123**, 6658-6670 (2018).
95. A. M. Rubin, J. P. Ampuero, Earthquake nucleation on (aging) rate and state faults. *Journal of Geophysical Research: Solid Earth* **110**, (2005).
96. R. A. Harris, M. Barall, B. Aagaard, S. Ma, D. Roten, K. Olsen, B. Duan, D. Liu, B. Luo, K. Bai, A suite of exercises for verifying dynamic earthquake rupture codes. *Seismological Research Letters* **89**, 1146-1162 (2018).
97. S. Wollherr, A.-A. Gabriel, C. Uphoff, Off-fault plasticity in three-dimensional dynamic rupture simulations using a modal Discontinuous Galerkin method on unstructured meshes: implementation, verification and application. *Geophysical Journal International* **214**, 1556-1584 (2018).
98. D. Roten, K. Olsen, S. Day, Y. Cui, D. Fäh, Expected seismic shaking in Los Angeles reduced by San Andreas fault zone plasticity. *Geophysical Research Letters* **41**, 2769-2777 (2014).
99. M. Dumbser, M. Käser, An arbitrary high-order discontinuous Galerkin method for elastic waves on unstructured meshes—II. The three-dimensional isotropic case. *Geophysical Journal International* **167**, 319-336 (2006).

100. A. Heinecke, A. Breuer, S. Rettenberger, M. Bader, A.-A. Gabriel, C. Pelties, A. Bode, W. Barth, X.-K. Liao, K. Vaidyanathan, in *SC'14: Proceedings of the International Conference for High Performance Computing, Networking, Storage and Analysis*. (IEEE, 2014), pp. 3-14.
101. S. Rettenberger, O. Meister, M. Bader, A.-A. Gabriel, in *Proceedings of the Exascale Applications and Software Conference 2016*. (2016), pp. 1-9.
102. C. Uphoff, S. Rettenberger, M. Bader, E. H. Madden, T. Ulrich, S. Wollherr, A.-A. Gabriel, in *Proceedings of the international conference for high performance computing, networking, storage and analysis*. (2017), pp. 1-16.
103. C. Pelties, A.-A. Gabriel, J.-P. Ampuero, Verification of an ADER-DG method for complex dynamic rupture problems. *Geoscientific Model Development* **7**, 847-866 (2014).
104. D. Andrews, Rupture models with dynamically determined breakdown displacement. *Bulletin of the Seismological Society of America* **94**, 769-775 (2004).
105. Y. A. Fialko, A. M. Rubin, What controls the along-strike slopes of volcanic rift zones? *Journal of Geophysical Research: Solid Earth* **104**, 20007-20020 (1999).
106. L. L. Erickson, "A three-dimensional dislocation program with applications to faulting in the earth", thesis, Stanford University (1986).
107. D. M. Boore, J. Watson-Lamprey, N. A. Abrahamson, Orientation-independent measures of ground motion. *Bulletin of the seismological Society of America* **96**, 1502-1511 (2006).
108. W. B. Joyner, D. M. Boore, Peak horizontal acceleration and velocity from strong-motion records including records from the 1979 Imperial Valley, California, earthquake. *Bulletin of the seismological Society of America* **71**, 2011-2038 (1981).
109. D. J. Wald, B. C. Worden, V. Quitoriano, K. L. Pankow, "ShakeMap manual: technical manual, user's guide, and software guide" (2005).
110. M. Pagani, D. Monelli, G. Weatherill, L. Danciu, H. Crowley, V. Silva, P. Henshaw, L. Butler, M. Nastasi, L. Panzeri, OpenQuake engine: An open hazard (and risk) software for the global earthquake model. *Seismological Research Letters* **85**, 692-702 (2014).
111. T. M. Brocher, Empirical relations between elastic wavespeeds and density in the Earth's crust. *Bulletin of the seismological Society of America* **95**, 2081-2092 (2005).

Acknowledgments:

We thank constructive comments by the editor Brent Grocholski and two anonymous reviewers. The facilities of IRIS Data Services, and specifically the IRIS Data Management Center, were used for access to waveforms, related metadata, and/or derived products used in this study. The GNSS data is provided by the General Directorate of Land Registry and Cadastre, and the General Directorate of Mapping, Turkey. IRIS Data Services are funded through the Seismological Facilities for the Advancement of Geoscience (SAGE) Award of the National Science Foundation under Cooperative Support Agreement EAR-1851048. We thank the Engineering Strong-Motion (ESM) Database by ORFEUS (*52*) for providing access to the data from the Turkish National Strong Motion Network, which is operated by Turkey's Disaster and Emergency Management Authority (AFAD). The computations in this study were supported by the supercomputer SuperMUC-NG.

Funding:

Funding for this work was provided by the National Science Foundation (EAR-2123529, EAR-1841273 to Y.F., EAR-2022441, EAR-2143413 to W.F., EAR-2121666 to A.A.G), the National Aeronautics and Space Administration (80NSSC22K0506 to Y.F., 80NSSC20K0495 to A.A.G.), the United States Geological Survey (G22AP00011 to P.S. and W.F.), and the Cecil and Ida Green Foundation. M.M., T.U. and A.A.G. were supported by the European Union's Horizon 2020 Research and Innovation Programme (TEAR grant No. 852992) and Horizon Europe (ChEESE-2P grant No. 101093038, DT-GEO grant No. 101058129 and Geo-INQUIRE grant No.101058518). J.R. was supported by the National Science Foundation Graduate Research Fellowship Program (grant No. DGE-2038238). A.A.G. gratefully acknowledges the Gauss Centre for Supercomputing e.V. (www.gauss-centre.eu) for providing computing time on the GCS Supercomputer SuperMUC-NG at Leibniz Supercomputing Centre (www.lrz.de), in project pn49ha.

Author contributions:

Z.Jia led the study, performed the subevent and kinematic slip inversions, and wrote the initial draft of the manuscript. Z.Jin, X.Z., and Y.F. processed the InSAR data, quantified the fault geometry, and performed static slip inversion. M.M., T.U., and A.A.G. performed the dynamic rupture simulations and the Coulomb failure stress analysis. W.F. performed back projection analysis and coordinated the collaboration. Y.F. conducted static Coulomb stress calculations. X.Z. contributed to the fault geometry determination and figure design. J.R., T.U., and A.A.G. conducted the ground motion analysis. F.B. and A.G. processed the GNSS data. W.F., P.S., A.A.G., Y.F. supervised the modeling and contributed to interpretation of the results. A.A.G., Y.F., and W.F. provided access to computational resources. All authors discussed the results and contributed to writing and revising the manuscript.

Competing interests:

Authors declare no competing interests.

Data and materials availability:

The Sentinel-1 SAR data are provided by the European Space Agency (ESA) and mirrored at the Alaska SAR Facility (ASF). The ALOS-2 PALSAR data are owned by the Japanese Space Agency (JAXA) and provided to Y.F. under a Research User Agreement.

The global seismic data are publicly available from the IRIS-DMC. The regional strong motion data are publicly available from the EMS Database by ORFEUS. The geodetic and seismic data, the data-driven slip models and subevent models, and the data required to reproduce the dynamic rupture earthquake sequence scenarios can be downloaded from https://doi.org/10.5281/zenodo.8128343 . We provide detailed README files summarizing the data and data formats provided.

Supplementary Materials

Materials and Methods

Figs. S1 to S28

Tables S1 to S2

References (*56–111*)

Movies S1 to S3

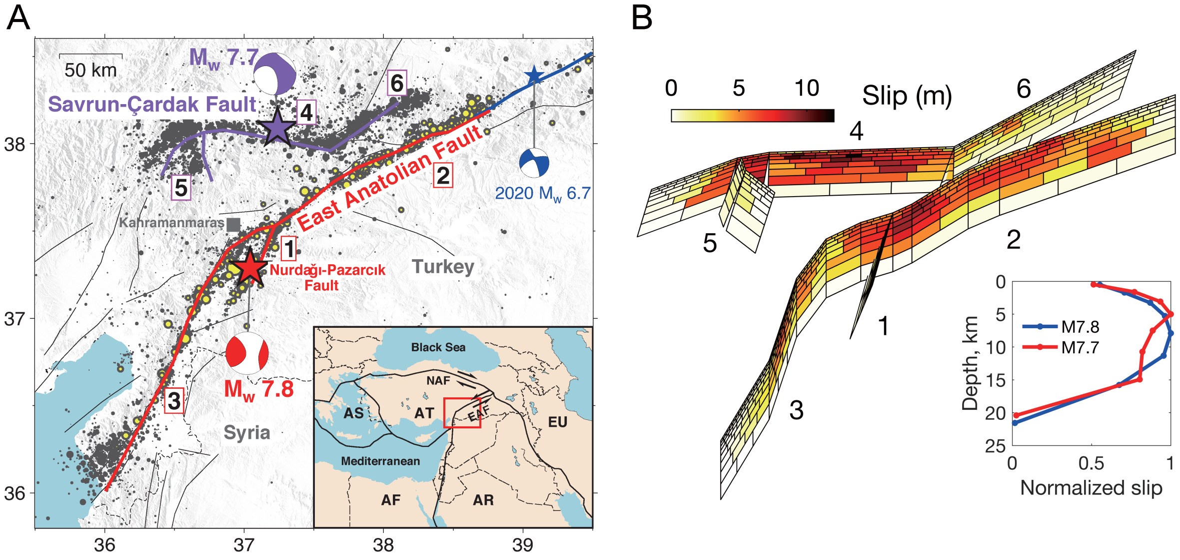

Fig. 1. A multi-fault earthquake doublet. (**A**) Tectonic background and aftershock seismicity of the study area near Kahramanmaraş, Turkey. Red and purple stars indicate the M_w 7.8 and 7.7 earthquake epicenters from the Turkey Disaster and Emergency Management Authority (*53*), and beachballs show focal mechanisms from the Global Centroid Moment Tensor catalog, respectively. Red and purple lines show surface ruptures identified from SAR data (*26*). Yellow dots show aftershocks for the period between the M_w 7.8 and 7.7 earthquakes and black dots are aftershocks following the M_w 7.7 event (*28*). The blue line and beachball denote the rupture extent and focal mechanism of the 2020 M_w 6.7 Elazig earthquake (*29*). Inset shows the regional tectonics and major plate boundary faults (solid black lines). Red outline denotes the study area. (**B**) Finite-fault model of the 2023 doublet derived from inversions of space geodetic (InSAR and GNSS) data. Fault segment numbers correspond to those shown in panel (A), in order of their rupture time: 1 - Nurdağı-Pazarcık Fault, 2 and 3 - East Anatolian Fault, 4-6 - Savrun-Çardak Fault. The inset panel shows the along-strike averaged coseismic slip normalized by the maximum slip amplitude, as a function of depth (*49*).

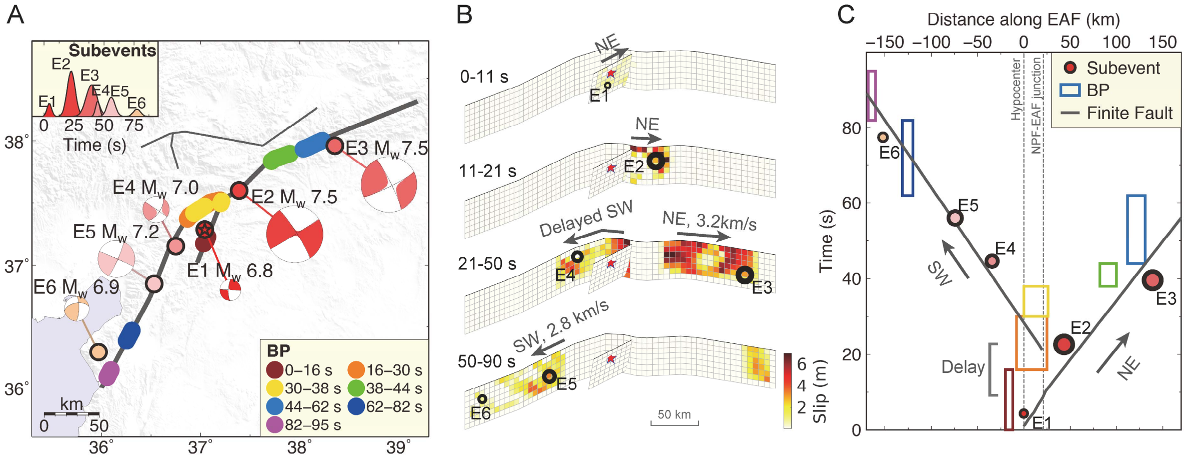

Fig. 2. Complex slip evolution of the M_w 7.8 earthquake, including delayed initiation of slip. (**A**) Subevent model from near- and far-field seismic observations and back-projection results, suggesting that the M_w 7.8 earthquake initiated on the NPF-1 (fault 1 in Fig. 1B), then propagated bilaterally, NE along the EAF-2 (fault 2) and SW along the EAF-3 (fault 3). The rupture of fault 2 terminates around 50 s, while rupture of fault 3 continues for an additional 30 s. (**B**) Rupture history within different time intervals from our kinematic slip inversion of far- and near-field seismic and geodetic data. We infer rupture velocities of 3.2 and 2.8 km/s for the NE and SW episodes, respectively, and a 10 s delay in the onset of the SW rupture along EAF-3 with respect to the NE rupture along EAF-2. The slip distribution within each time interval agrees with the subevent (black circles) inversion. (**C**) Subevents, back-projection locations and times, and finite-fault velocities (in B) consistently indicate delayed initiation of slip on branch EAF-3.

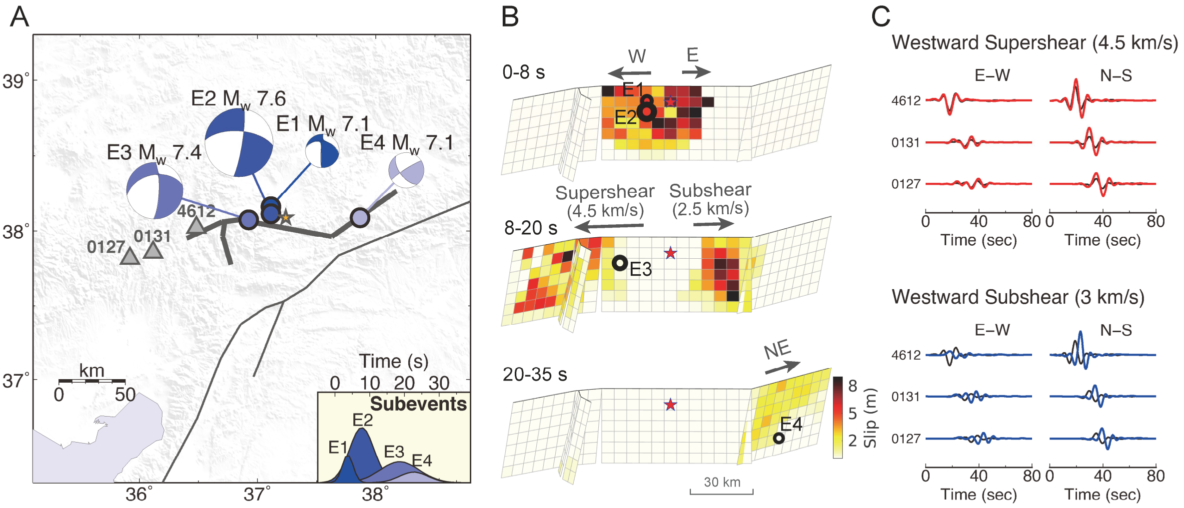

Fig. 3. Asymmetric kinematics of the *M$_w$* 7.7 earthquake. (**A**) Three subevents close to the hypocenter suggest a bilateral rupture. The fourth event images the rupture of the Doğanşehir branch (fault 6 in Fig. 1B). (**B**) Asymmetric bilateral rupture velocities of the *M$_w$* 7.7 event. The westward rupture has an inferred supershear velocity of 4.5 km/s, whereas a subshear velocity is seen towards the east (2.5 km/s). Note that subevent locations are based on their seismic moment centroids. The slip may not be the largest at the centroid location, specifically for bilateral ruptures. For example, E3 (10-30 s) averages slip pulses of both the westward supershear and the eastward subshear rupture. (**C**) A westward supershear rupture velocity (red waveforms) better explains observed waveforms (black) at near-fault strong motion stations to the west (triangles in A) than a subshear rupture (blue).

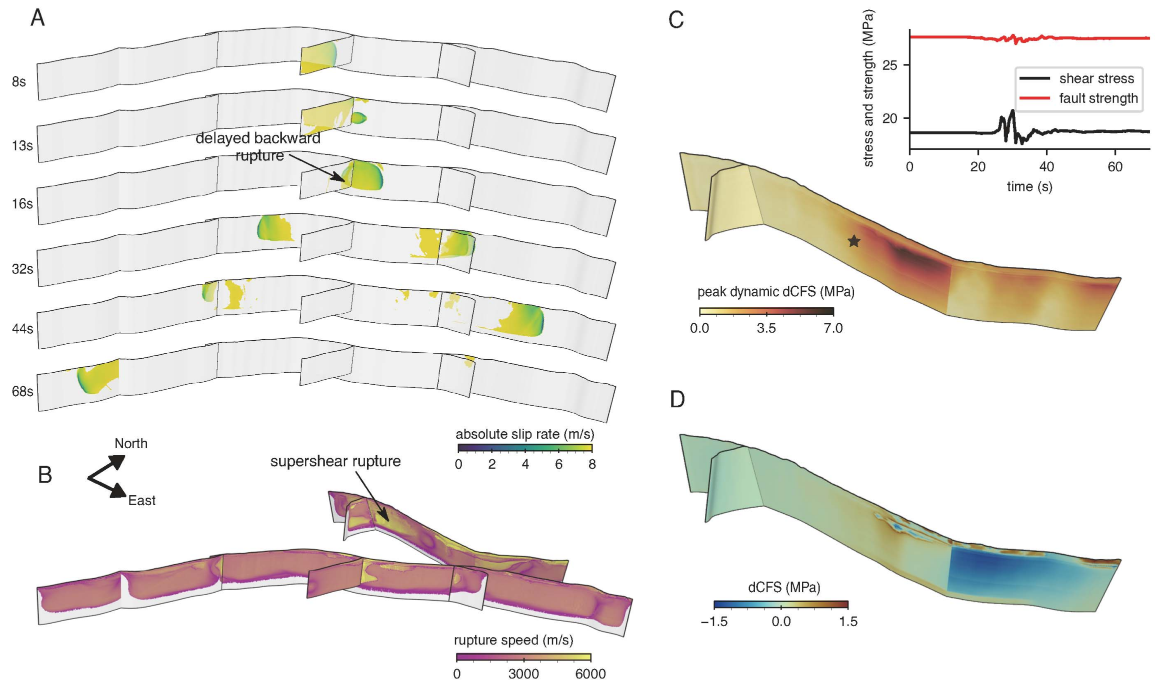

Fig. 4. 3D dynamic rupture scenarios and stress-mediated interactions of the M_w 7.8 and 7.7 earthquakes. (**A**) Snapshots of absolute slip rate evolution in the M_w 7.8 dynamic rupture scenario (Video S1). (**B**) Modeled rupture speeds in linked dynamic rupture simulations (*54*) of both earthquakes indicating dominantly sub-shear rupture speeds but sustained westward supershear during the M_w 7.7 scenario (Fig. S21, Video S2). (**C**) Peak absolute dynamic shear stress perturbation reaching up to 7 MPa measured in the direction of maximum initial traction. Inset: Evolution of dynamic shear stress and fault strength at the M_w 7.7 hypocenter (black star). (**D**) Static Coulomb failure stress changes ΔCFS assuming a static friction coefficient of 0.6.

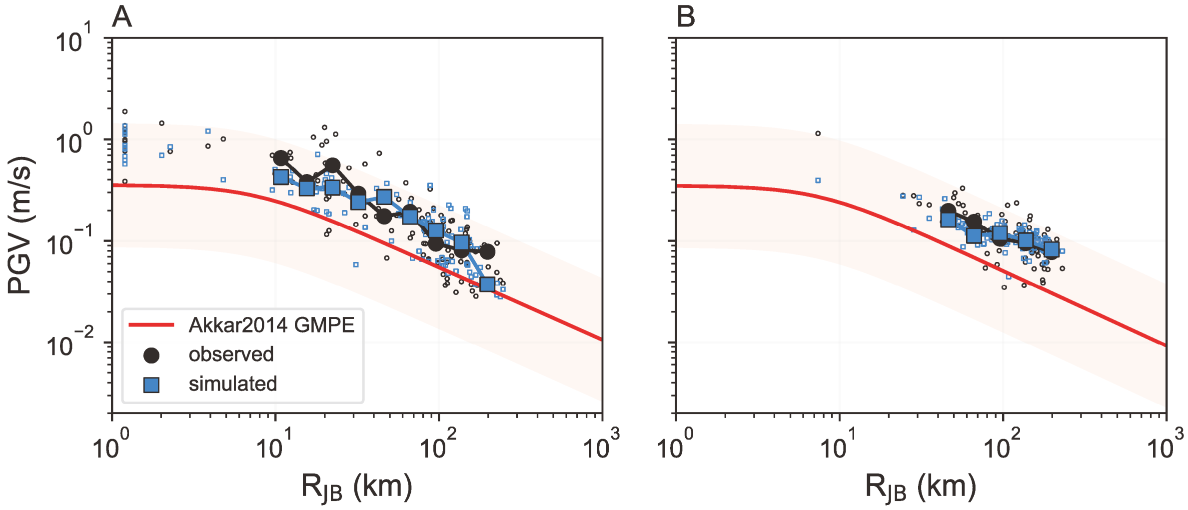

Fig. 5. Peak ground velocities (PGV) plotted against Joyner-Boore distance (R_{JB}) for the M_w 7.8 (A) and M_w 7.7 (B) earthquakes. Observed PGVs from strong motion accelerometers are indicated by open black circles, and simulated PGVs from the dynamic rupture simulations are indicated by open blue squares. We bin the PGV data by R_{JB} and plot the medians for each distance bin (solid markers). The red curve indicates PGV predicted by a ground motion model (*55*) assuming an average shear wave velocity for the top 30 m of soil (VS_{30}) of 760 m/s, with the shaded area denoting its uncertainty. All PGV are rotationally independent geometric mean values (GMRotD50). We include simulated and observed data at the same locations, respectively.

Science
AAAS

Supplementary Materials for

The complex dynamics of the 2023 Kahramanmaraş, Turkey, M_w 7.8-7.7 earthquake doublet

Zhe Jia[1*], Zeyu Jin[1], Mathilde Marchandon[2], Thomas Ulrich[2], Alice-Agnes Gabriel[1,2], Wenyuan Fan[1], Peter Shearer[1], Xiaoyu Zou[1], John Rekoske[1], Fatih Bulut[3], Asli Garagon[3], Yuri Fialko[1]

Corresponding author: z5jia@ucsd.edu

The PDF file includes:

Materials and Methods
Figs. S1 to S28
Tables S1 to S2
Videos S1 to S3
References

Materials and Methods

InSAR and GNSS observations

We use Synthetic Aperture Radar (SAR) data acquired by the L-band ALOS-2 satellite operated by the Japan Aerospace Exploration Agency (JAXA), and the C-band Sentinel-1A satellite operated by the European Space Agency (ESA). ALOS-2 data that cover the earthquake area include acquisitions from ascending tracks 183, 184, 185, (frames 700 and 750) and descending tracks 76, 77, and 78 (frames 2850 and 2900) made in the ScanSAR mode, and from descending track 78 made in the stripmap mode. Sentinel-1A data are acquired from ascending tracks 14, 116, and descending track 21 in TOPS mode. The respective acquisition dates are listed in Table S1.

Because of the large amplitude of coseismic slip (on the order of 10 m) and extensive surface disruption, Sentinel-1 interferograms are highly decorrelated within 10-20 km from the fault traces. Therefore, we use Sentinel-1 SAR data to calculate pixel offsets by cross-correlating the radar amplitude of full-resolution Single Look Complex (SLC) images taken before and after the M_w 7.8–7.7 earthquakes. To avoid biases due to excessive filtering and averaging, especially across the fault trace, we use the raw offsets. To reduce the data scatter, we remove outliers by calculating the difference between the raw and filtered offsets. Pixels for which the difference exceeds 1 m are masked out. We do not use the azimuth offsets due to the large pixel size in the azimuth direction (~14 m), resulting in a low signal-to-noise ratio. Sentinel-1 range offsets used in our inversions are shown in Fig. S1g-i. For ALOS-2 data, we produce both interferograms (ScanSAR mode, Fig. S1a-f) and pixel offsets (stripmap mode, Fig. S1j,k).

All SAR data are processed using GMTSAR (*56*). Contributions to radar phase due to topography are removed using the SRTM digital elevation model (*57*). Interferograms are unwrapped using the branch-cut method (*58*). Because ALOS-2 L-band data are susceptible to ionospheric noise, we correct the latter by fitting a linear ramp to the far-field line of sight (LOS) displacements, and subtracting the respective ramps from the affected interferograms. We quality-check the data, and manually mask out identified near-field unwrapping errors in ALOS-2 interferograms (Fig. S1j,k).

We also use observations from continuous Global Navigation Satellite System (GNSS) sites located within 500 km from the epicentral area. In total, twenty-six GNSS stations are used from the CORS-TR network operated by the General Directorate of Land Registry and Cadastre, and the General Directorate of Mapping (Fig. S7). The data are sampled at 30 s intervals. The cutoff for the elevation angle is set to 10 degrees. Ten days of data are analyzed framing the mainshocks, five days before and five days after. Each day is treated as a single epoch to have the best possible accuracy except for the day of mainshocks (Feb 6, 2023). The nine hours between the two mainshocks are used to represent another epoch to differentiate between surface displacements due to each event.

The GNSS data are processed using the GAMIT/GLOBK software package in Precise Point Positioning mode (*59*). Fourteen IGS stations are used to achieve stabilization based on the ITRF 2014 reference frame. IGS orbits are obtained from the Scripps Orbit and Permanent Array Center (SOPAC, http://sopac-csrc.ucsd.edu). Earth orientation parameters are obtained from the

United States Naval Observatory (USNO, http://usno.navy.mil). The elevation-dependent model is applied for the receiver antenna phase center calibrations. The L1 and L2 carrier phases are combined linearly independent from the Ionosphere (LC) to eliminate the ionospheric delay. Tropospheric delays generated by the temperature, pressure, and humidity are minimized using the Global Mapping Function model in 2-hour intervals (*60*). The FES2004 Ocean Tide Loading (OTL) global grid is used to simulate ocean tides (*61*). IERS2003 is used to simulate the Earth and pole tide models (*62*).

We use Sentinel-1 range offsets, ALOS-2 interferograms, range and azimuth offsets from different lines of sight, and coseismic GNSS displacements to constrain the static slip distribution due to the M_w 7.8-7.7 events. Because the events occurred within a short period of time, SAR data capture combined displacements due to the two events. The GNSS vector displacement data are however available for each event individually, as well as for the two events combined. The computed pixel offsets are used to map the rupture traces and, in combination with precisely located aftershocks (*28*), to constrain the sub-surface rupture geometry (*27*). Based on this analysis, we model the EAF as a vertical fault, the Nurdağı-Pazarcık Fault (NPF, fault 1 in Fig. 1A) as dipping to the northwest at 70 degrees, and the M_w 7.7 rupture (the Savrun-Çardak Fault) as dipping to the north at 70 degrees. In our joint inversion, we assign relative weights of 1 to the interferograms and GNSS data, 0.6 to range offsets, and 0.2 to azimuth offsets.

For computational efficiency and better model resolution, each coseismic displacement map is sub-sampled using an iterative quad-tree sampling algorithm (*63*). Given the patch length of ~2 km in the shallowest part of the slip model, we sample the near-field data with a minimum spacing between the data points of about 300 to 400 meters. The unit-look vectors are computed by averaging the original values in the same groups of pixels as used for sub-sampling the phase and pixel offset data.

We extend the rectangular segments approximating the fault geometry to a depth of 30 km and several kilometers along the fault strike beyond the mapped fault traces. Each segment is divided into patches with sizes that increase with depth in a geometric progression to ensure that the model resolution matrix is close to diagonal (*64*). We apply positivity constraints to the strike-slip components, such that slip is constrained to be left-lateral on most of the fault segments, except for segment 5 of the Mw 7.7 rupture (see Fig. 1B) which is allowed to be right-lateral. The dip-slip components are unconstrained. To prevent large variations in slip between neighboring fault patches, we apply continuity constraints (which on a regular grid are equivalent to minimizing the first spatial derivative of slip). We further impose a “soft” zero-slip boundary condition at the fault edges, except at the Earth’s surface (*27*).

The inversions are performed using the Green’s functions for both a homogeneous and layered elastic half-space (*65*). Unless noted otherwise, results presented in this manuscript correspond to layered elastic half-space models. We estimate the depth distribution of elastic moduli of the layered half-space from the 3D seismic tomography models (*23*). Inversions in which the fault dip angle was allowed to vary confirm a 70-degree northward dip for the M_w 7.7 fault rupture, a 70-degree westward dip for the Nurdağı-Pazarcık Fault that initiated the M_w 7.8 event, and a vertical dip on all ruptured sections of the EAF. Figs. S3–S6 show the sub-sampled data, predictions of the best-fit models and residuals for the data sets used in the inversion. Overall, our preferred model (Figs. 1B and S2) fits the main features of the displacement field well, with a variance reduction of more than 96% for the interferograms and 75% for the pixel offsets. We compute the seismic moment for each event by summing up scalar seismic moments of the respective slip patches (Figs. 1B and S2). Inversions using a homogeneous half-space give rise to the moment magnitudes of 7.83 and 7.70 for the first and second event, respectively, assuming the shear modulus of 33 GPa. Inversions using a layered half-space give rise to the moment magnitudes of 7.89 and 7.74 for the first and second event, respectively, assuming the depth-dependent shear modulus from our layered model. Fig. S7 shows a comparison between GNSS observations and model predictions for each event. Since the static slip model was derived from data spanning both events, a good agreement between the data and model predictions for individual events (Fig. S7) indicate that the latter are well resolved and trade-offs between coseismic displacements due to individual events in our inverse models are minimal. We note that models assuming a layered elastic half-space do a better job fitting both the near- and far field GNSS data compared to models assuming a homogeneous elastic half-space, in agreement with studies of other large earthquakes (*26*).

Subevent inversion

We apply a subevent inversion method (*30, 31*) to simultaneously constrain a total of 6 subevents for the M_w 7.8 earthquake and 4 subevents for the M_w 7.7 earthquake. We determine the number of subevents by iteratively adding subevent numbers in the inversions until the waveforms are well fit and the total moment is consistent with the long-period moment from the geodetic solutions. The major advantage of the subevent inversion method is that it can describe multi-fault rupture processes with flexible subevent locations, timings, and focal mechanisms, without imposing strong assumptions on the fault geometry or rupture velocity.

Each subevent has 10 unknown source parameters, including the horizontal location and depth, centroid time, centroid duration, and 5 deviatoric moment tensor components. Our two-stage algorithm allows us to search for part of these parameters nonlinearly and invert the data for the other parameters using a linear approach, which substantially improves the inversion efficiency. In the outer (first) stage, we use a Metropolis-Hasting Markov Chain Monte Carlo (MCMC) sampler to drive the search for nonlinear parameters, including subevent locations, timings, and source durations. In each MCMC sampling step, we perturb one of the nonlinear parameters while keeping the other nonlinear parameters at their current values (*66*), which ensures a high acceptance rate and sampling efficiency. Given the set of nonlinear parameters in the inner (second) stage, we linearly invert the seismic data for the moment tensors by extending their linear relationship (*67*) to multiple sources. Ultimately, the MCMC sampler only needs to search 5 nonlinear parameters for each subevent, which clears the path to extensively explore the model space.

We generate 192 Markov Chains and eventually keep the best 48 for each inversion, to avoid the chains being trapped in local minima. Our MCMC inversion incorporates a Bayesian framework that accounts for data errors and model priors to estimate the model uncertainties. We assign bounded uniform prior distributions of all nonlinear parameters except the horizontal locations, for which we set priors based on the aftershock distributions. Although the actual noise and instrumental errors for the seismic waveforms are minimal, we empirically introduce a data error of 10% of the misfit to address inaccurate assumptions of the wave propagation processes

(Green's function). The model uncertainties are ultimately represented by the widths of the Markov Chain sample distributions, which are equivalent to the posterior probability density functions.

We incorporate a variety of datasets, including P waves of 63 teleseismic (epicentral distance between 30°-90°) stations in displacement and velocity, SH waves of 66 teleseismic stations in displacement, and three-component full waveforms in velocity recorded by 78 local (epicentral distance within 200 km) strong ground motion stations (Fig. S9-S13). The data are selected from the Global Seismic Network (GSN), the International Federation of Digital Seismograph Network (FDSN), as well as the Turkish National (TK) strong ground motion network for good quality and azimuthal coverage. The weighting of these datasets is set to be 5, 1, and 0.0015 for similar contributions to the final misfit. We remove the instrument responses and the linear trends of these data. For the teleseismic data, we rotate the two horizontal components to the radial and transverse components, and we apply a 0.005–0.15 Hz band-pass filter. For the local strong ground motion data, we apply a 0.02–0.15 Hz filter. To account for path effects and picking errors, we allow a time shift up to 2s for teleseismic P waves, 5s for teleseismic SH waves, and 2s for the regional strong motion data. We calculate Green's functions using the 1D velocity model of Güvercin et al. (*23*) for the crust (Table S2) and the IASPEI91 model (*68*) for the deeper earth. We compute teleseismic Green's functions with a hybrid method that combines a propagator matrix and ray theory (*69, 70*), and calculate local Green's functions based on the frequency-wavenumber integration method (*71*).

The seismicity locations and the space geodesy data tightly constrain the fault geometry and surface ruptures, which provides our subevent inversion with useful priors. For the M_w 7.8 earthquake, we incorporate the horizontal spatial density of its early aftershocks before the M_w 7.7 event as the prior distribution for the subevent locations. We also fix the location of the first subevent to be at the hypocenter on the NPF, which is well constrained by the InSAR data. For the M_w 7.7 earthquake, we impose the horizontal spatial density of its aftershocks as the prior for the subevent locations, and anchor the last subevent at the location where the slip patch on the Doğanşehir branch is observed in the static slip model. Fixing the location of one subevent avoids all subevents moving their horizontal locations together with the seismograms shifting simultaneously, thus stabilizing the inversion. The narrow subevent model uncertainty limits for the M_w 7.8 and 7.7 events reveal that their subevent models are well constrained by the data.

Back projection

We employ a standard time-domain back-projection method (*32, 72*) to analyze the rupture propagation of the M_w 7.8 earthquake. This technique has been widely used to detect aftershocks and resolve earthquake radiation patterns because it does not make many assumptions about the fault geometry or rupture velocity (*9, 73*). Back-projection has successfully investigated the spatiotemporal evolution of complex earthquakes, such as multi-fault rupture events and supershear earthquakes (*74, 75*).

We collect P-wave velocity records of the event from all seismic stations within an epicentral distance range of 30° to 90°. We apply a 0.05–0.5 Hz fourth-order Butterworth filter to the data and remove records with signal-to-noise ratios (SNR) of less than 3. The SNR is calculated as the root-mean-square (RMS) amplitude ratio from time windows 10 s before and after the theoretical P-wave arrival obtained from the International Association of Seismology and Physics of the Earth's Interior (IASP91) travel-time tables (*68*). To eliminate any effects of stations located close to the nodal plane directions, we exclude them from the analysis. We visually inspect the records and select only those with clear P-wave onsets. Traces with positive polarities are also discarded. After quality control, we align the traces using multi-channel cross-correlation with a time window from -2 to 6 s relative to the theoretical P arrivals. Polarity flips are not allowed during cross-correlation. In total, we use 391 stations to image the rupture evolution of the M_w 7.8 earthquake, as shown in Fig. S15.

The back-projection procedure first predefines a set of points for potential sources around the earthquake hypocenter, with a fixed horizontal point spacing of 10 km at the hypocentral depths (Point-set 1). The potential source point spans an area of 600 km by 600 km, with the earthquake epicenter located at the center of the points. To improve the spatial resolution of the back-projection images, we employ a *N*th root stacking (N=4) method, albeit at the cost of losing absolute amplitude information (*76, 77*). We normalize the records using their peak amplitudes and inversely scaling by the number of contributing stations within 5° to balance the azimuthal and spatial coverage of the stations. To evaluate the spatiotemporal migration, we generate back-projection snapshots using different stacking windows to balance the trade-off between resolution and robustness (Fig. S15). We normalize the back-projection snapshots by the maximum power within each window and present them as contours with coherence exceeding 90% of the maximum normalized energy (Fig. S15). The back-projection snapshots exhibit good agreement with the fault traces. Since the event displays simple linear rupture propagation, we estimate the average rupture speed of various rupture branches to be approximately 3 km/s for the M_w 7.8 earthquake.

The M_w 7.8 earthquake ruptured a group of nearly vertical strike-slip faults, and space geodetic observations enable us to accurately define the fault traces. To limit the potential sources, we restrict them to be along the fault traces (Point-set 2) for the back-projection analysis. We adopt the same stacking procedure using the same set of P waves as in Point-set 1. The results, presented in Fig. 2, include snapshots with varying window lengths that help to infer the earthquake rupture propagation. The back-projection images are robust and in agreement with those obtained using Point-set 1.

Kinematic slip inversion

We conduct a joint kinematic slip inversion of the M_w 7.8 and 7.7 earthquakes using both seismic and geodetic data, following the finite-fault inversion framework of Jia et al. (*33*). We used the same fault geometry as used in the static slip inversion (Figs. 1B, S2). The rake angles are constrained by the corresponding subevent focal mechanisms (rake angles of fault 1-6: 0°, 8°, 0°, -10°, 180°, 40°). We discretize each fault segment into subfault grids with horizontal and depth intervals of 6 km and 4 km, respectively. Each subfault grid has a triangle moment rate function with a duration of 4 s.

For both events, we use one rupture velocity per fault segment, and calculate the rupture time of each subfault patch based on its in-plane distance from the grid of initial rupture (i.e., the epicenter on the first segment), which is effectively a slip-pulse rupture expansion. For bilateral rupture scenarios, estimation of rupture velocity based on subevent locations may be biased.

Through grid-searching (Fig. S18), we obtain the optimal rupture velocities of 3.2 km/s to the northeast and 2.8 km/s to the southwest for the M_w 7.8 earthquake. Notably, a delay for the nucleation of the southwest segment is required by the data, and we find the optimal delay time is 10 s (Fig. S17). For the M_w 7.7 earthquake, we obtain an eastward rupture velocity of 2.5 km/s, whereas we constrain a westward supershear rupture with an optimal velocity of 4.5 km/s (Fig. S19). Unlike the M_w 7.8 event, we do not find that any delayed rupture branches occurred during the M_w 7.7 earthquake.

Once we define the fault geometries, rake angles, and rupture times, the slip amplitudes are the only remaining unknown parameters. We extend the linearized finite-fault inversion method of Hartzell and Heaton (*78*) to model the two earthquakes in a single inversion. We use a combination of regional strong ground motions, teleseismic P and SH waves in displacement, two tracks of ALOS-2 ScanSAR line-of-sight displacements, and the Sentinel-1 ascending and descending range offsets. Processing and filtering of the seismic data and the Green's functions follows the same procedures as the subevent inversion described above, but we do not allow any time shifts for the local strong motion waves to avoid trade-offs between time-shifting and rupture velocity estimates. Processing of the InSAR data follows the previous static slip inversion. InSAR Green's functions are calculated using the same 1D velocity model of Güvercin et al. (*23*) with a frequency-wavenumber integration method (*71*).

We set up a linear system describing the relationship between observed data and the subfault synthetics,

$$\begin{bmatrix} G^{1}_{SM\_7.8} & G^{2}_{SM\_7.8} & \cdots & G^{k}_{SM\_7.8} & 0 & 0 & \cdots & 0 \\ G^{1}_{TelP\_7.8} & G^{2}_{TelP\_7.8} & \cdots & G^{k}_{TelP\_7.8} & 0 & 0 & \cdots & 0 \\ G^{1}_{TelSH\_7.8} & G^{2}_{TelSH\_7.8} & \cdots & G^{k}_{TelSH\_7.8} & 0 & 0 & \cdots & 0 \\ 0 & 0 & \cdots & 0 & G^{1}_{SM\_7.7} & G^{2}_{SM\_7.7} & \cdots & G^{l}_{SM\_7.7} \\ 0 & 0 & \cdots & 0 & G^{1}_{TelP\_7.7} & G^{2}_{TelP\_7.7} & \cdots & G^{l}_{TelP\_7.7} \\ 0 & 0 & \cdots & 0 & G^{1}_{TelSH\_7.7} & G^{2}_{TelSH\_7.7} & \cdots & G^{l}_{TelSH\_7.8} \\ G^{1}_{InSAR\_7.8} & G^{2}_{InSAR\_7.8} & \cdots & G^{k}_{InSAR\_7.8} & G^{1}_{InSAR\_7.7} & G^{2}_{InSAR\_7.7} & \cdots & G^{l}_{InSAR\_7.7} \end{bmatrix} * \begin{bmatrix} m^{1}_{7.8} \\ m^{2}_{7.8} \\ \vdots \\ m^{k}_{7.8} \\ m^{1}_{7.7} \\ m^{2}_{7.7} \\ \vdots \\ m^{l}_{7.7} \end{bmatrix} = \begin{bmatrix} d_{SM\_7.8} \\ d_{TelP\_7.8} \\ d_{TelSH\_7.8} \\ d_{SM\_7.7} \\ d_{TelP\_7.7} \\ d_{TelSH\_7.7} \\ d_{InSAR\_both} \end{bmatrix}$$

in which $\boldsymbol{m}^{\boldsymbol{1}\cdots\boldsymbol{k}}_{\boldsymbol{7.8}}$ and $\boldsymbol{m}^{\boldsymbol{1}\cdots\boldsymbol{l}}_{\boldsymbol{7.7}}$ are the slip vectors of all subfault grids for the M_w 7.8 and M_w 7.7 earthquakes, respectively, $\boldsymbol{d}_{[\boldsymbol{data\ type}]\_[\boldsymbol{event}]}$ is the data vector including a variety of data types (Strong motion, teleseismic P and SH waves, and InSAR). $\boldsymbol{G}^{\boldsymbol{1}\cdots[\boldsymbol{k\ or\ l}]}_{[\boldsymbol{data\ type}]\_[\boldsymbol{event}]}$ represents the synthetics of different data types for unit slip on the corresponding subfault grids. For the seismic data, both $\boldsymbol{G}$ and $\boldsymbol{d}$ are time series of all stations from end to end, and they are linked to the M_w 7.8 and 7.7 earthquakes independently. The InSAR data and Green's functions are formatted as gridded surface line-of-sight (LOS) displacements and they span both earthquakes. Therefore, the seismic data helps to differentiate the slip distribution for these two events, while the InSAR data provide constraints on their total slip. We can directly resolve the least-square slip distributions of the two earthquakes, but the result is unstable because of ill-conditioning of this inverse problem. To stabilize the inversion, we introduce four types of constraints, including 1) non-negative constraints on the slip, 2) minimization of the slip differences between adjacent subfault grids, 3) penalizing slip at the non-surface boundaries of the faults, and 4) minimizing the L2 norm of the slip distribution (*78, 79*). These constraints help to avoid unphysical solutions (negative slip, enormous strain, etc.) and overfitting. To flexibly incorporate these constraints, we used the CVX optimization algorithm (*80*) to solve our inverse problem.

Dynamic rupture simulations

Dynamic rupture models require prescribed initial conditions, including fault geometry, relative fault strength, prestress, and material properties (*81, 82*). Our dynamic rupture simulations use the same model setup for linked forward simulations of both earthquakes (*54*). We inform our initial parameterization from observations: fault geometry from geodesy and seismicity, large-scale fault loading from regional seismo-tectonics and smaller-scale stress heterogeneity from static slip inversion, and fault strength from first-order earthquake kinematics. We prescribe larger fracture energy, larger nucleation area, and closer to critically stressed faults for the second event to capture its rupture dynamics which are distinct from the first earthquake (see main text).

Fault geometries:

We account for the large-scale geometrical complexities of the fault system, including fault bends and secondary segments. Our dynamic rupture model includes the faults hosting both events and the relative effects of the static and dynamic stresses of the M_w 7.8 event on the dynamics of the second earthquake. We include ten curved, intersecting segments of the EAF and SCF (Fig. S20) as inferred from geodetic analysis and resembling the fault geometries of the static and kinematic models. We extend mapped surface fault traces to a depth of 20 km with varying dip angles ranging between 90° for all EAF segments and 70°N for the main segments of the second event. The minor Göksun splay (segment 5, Fig. 1) is dipping 90°.

Fault friction and relative fault strength:

We use the widely used linear slip-weakening friction law (*83*), with static friction coefficient μ_s=0.6 and dynamic friction coefficient μ_d=0.2 on all faults. The critical slip distance varies between D_c= 0.5 m for faults hosting the first earthquake and for the Göksun splay, and D_c= 1.0 m, implying larger fracture energy for the main faults hosting the second event.

S, the ratio of initial strength excess to nominal stress drop (*84*), is a measure for the relative strength of faults in dynamic rupture simulations. While static and dynamic friction coefficients are constant on all faults, we find that prescribing variable relative fault strength *S* is required to dynamically reproduce the first-order earthquake kinematics, such as moment magnitude and rupture extent. *S* varies due to variable prestress (next section). Furthermore, the local fault geometry modulates the prescribed regionally variable relative fault strength (Fig. S20), implying that locally more optimally oriented fault portions are closer to critically prestressed.

Prestress:

We combine large-scale variability in fault loading inferred from regional seismo-tectonics and modulated by fault geometry with small-scale heterogeneity inferred from static slip inversion. We assume depth-dependent effective normal stress and combine shallow mildly overpressurized pore fluids, with a pore fluid pressure of $\boldsymbol{\gamma}=\boldsymbol{\rho}_{\text{water}}/\boldsymbol{\rho} = 0.66$, with effectively constant effective normal stress below ~ 6km (*85-87*).

Following previous dynamic rupture simulations unraveling complex multi-fault earthquakes (*12, 54, 88, 89*), we constrain large-scale variability in fault loading from regional seismo-tectonic observations (Fig. S20). Here we combine stress inversion (*23*), InSAR constrained principal strain rate orientations (*90*), with recent focal mechanisms (AFA, https://deprem.afad.gov.tr/event-focal-mechanism) to prescribe an along-strike rotating prestress state, which is required to dynamically reproduce rupture dynamics of both earthquakes. Specifically, we find that close-to-optimal loading of the central segment of the second earthquake reproduces its observed large slip and surface displacements.

Small-scale variability of dynamic rupture parameters cannot be measured in situ and is difficult to constrain. Dynamic source inversions for friction parameters and the initial state of fault stress (*91, 92*) are limited to sufficiently simple dynamic rupture models due to the computational cost of the forward problem. We derive the spatially-variable static stress changes associated with our geodetically inferred static-slip model using the same computational model as the dynamic rupture models. In a pseudo-dynamic calculation, we impose the geodetic slip model and measure the associated stress heterogeneity (*37*) in the full stress tensor.

Inferring initial stresses directly from data-driven slip models (*93, 94*) often requires additional assumptions and ignores regional tectonic constraints. We combine large-scale and small-scale prestress heterogeneities based on a few trial dynamic rupture scenarios. We find that balancing their respective amplitudes using a scaling factor of 0.65 for the smaller-scale stress changes and S ratios varying between 0.54 and 2.33 (Fig. S20) spontaneously reproduces earthquake kinematics, geodetic deformation and ground motions of both events very well (Figs. S21-S25).

Nucleation:

We initiate both ruptures by linearly decreasing static frictional strength $\mu_s=0.6$ to μ_d in two separately-activated gradually expanding nucleation patches of maximum sizes 2 km (M_w 7.8) and 3 km (M_w 7.7) centered at the same respective hypocenter locations as in the kinematic model and observationally inferred from AFAD (*53*). Only a critical portion (*95*) of the fault needs to reach failure to nucleate rupture, while other parts of the faults are prestressed well below critical and yet break dynamically. We use a nucleation patch smoothly varying in space and time (*96*) and acting across a minimal-sized perturbation area, avoiding artifacts when initiating self-sustained spontaneous rupture with minimal perturbation determined in several trial dynamic rupture simulations.

Material properties and dynamic rupture model domain:

We embed all faults in the same 1D velocity model as the data-driven models (*23*), which does not include viscoelastic attenuation. Our dynamic rupture model domain accounts for high-resolution (450 m) topography from SRTM DEM data (*57*). We assume a depth-dependent, non-associated Drucker-Prager elasto-viscoplastic rheology to model coseismic off-fault plastic deformation (*97*). We parameterize off-fault plasticity by bulk internal friction coefficient and 3D variable plastic cohesion. We use a uniform bulk friction coefficient of 0.6, matching our on-fault static friction coefficient, and define plastic cohesion C_{plast} as proportional to the 1D depth-dependent shear modulus μ in [Pa] following Roten et al. (*98*), as:

$$C_{\text{plast}} = 2 \times 10^{-4} \max(\mu(z), 2 \times 10^{10}).$$

We taper bulk cohesion at depths shallower than 2 km, where confinement stresses are low.

Numerical method:

We solve the spontaneous dynamic rupture problem with high-order accuracy in space and time using the open-source software SeisSol (www.seissol.org). SeisSol uses the Arbitrary high-order accurate DERivative Discontinuous Galerkin method (ADER-DG) (*99*) and end-to-end optimization for high-performance computing infrastructure (*100-102*). SeisSol employs fully non-uniform unstructured tetrahedral meshes that statically adapt to geometrically complex 3D geological structures, such as non-planar, intersecting faults, and topography. SeisSol has been verified in various community benchmarks (*96, 103*).

We spatially discretize our model domain in an unstructured tetrahedral mesh consisting of 33 million tetrahedral elements. The mesh is statically adapted to resolve frequencies of at least 1 Hz everywhere, acknowledging the 1D seismic velocity model. We choose a maximum element edge-length of 300 m at all fault interfaces. The size of the area behind the rupture front where shear stress decreases from its static to its dynamic value is the process zone width (*104*). We here measure the median process zone width as 750 m. The recommended number of elements required to resolve the median process zone size in a SeisSol dynamic rupture simulation setup with off-fault plasticity and heterogeneous initial stress conditions is 2 for our chosen polynomial order of basis functions p = 4 (*97*). Thus, our rupture models are well resolved by our chosen discretization, noting that each dynamic rupture element provides sub-element resolution.

We spatially discretize our model domain in an unstructured tetrahedral mesh of 31 million tetrahedral elements. The mesh is statically adapted to resolve frequencies of at least 1 Hz everywhere in a high-resolution area of 400 km × 200 km with the NE-SW main axis aligned with the fault system, acknowledging the 1D seismic velocity model at depth. In larger distances to the faults, mesh resolution adaptively coarsens. We still resolve 0.25 Hz at the edges of the dynamic rupture model domain which spans a total extent of 600 km × 600 km × 500 km. We choose a maximum element edge-length of 300 m at all fault interfaces. The size of the area behind the rupture front where shear stress decreases from its static to its dynamic value is the process zone width (97). We here measure the median process zone width as 5300 m (90). Our rupture models are well resolved by our chosen spatial and temporal discretization, which includes basis functions of polynomial order p = 4, noting that each dynamic rupture element provides sub-element resolution.

ΔCFS and ΔCFD calculations:

We compute ΔCFS or ΔCFD across the SCF fault system from the dynamic rupture simulation of the M_w 7.8 earthquake, which allows us not to be restricted to an a priori assumed planar fault geometry but to use a full cartesian tensor and account for the full complexity of the fault network when resolving on-fault stress changes. We calculate the M_w 7.8 static Coulomb failure stress changes ΔCFS at 150 s after initiating the first dynamic rupture simulation, which ensures that transient seismic waves have left the model domain. We measure ΔCFS in the direction of maximum shear tractions at each point of the complex fault system as $\Delta CFS = \Delta\tau - f\,\Delta\sigma_n$, with $\Delta\tau$ and $\Delta\sigma_n$ being the dynamic shear and normal fault stress changes, and $f = \mu_s = 0.6$ the static friction coefficient used in the dynamic rupture simulations. We measure the absolute dynamic Coulomb failure stress perturbation (ΔCFD) in the direction of maximum initial traction throughout the rupture time of the first event's dynamic rupture scenario. We show its maximum values across the SCF fault system in Fig. 4C of the main text.

To investigate the sensitivity of the computed static stress changes to uncertainties in the orientation of the nucleation site of the M_w 7.7 event, we compute shear and normal stress perturbations caused by the M_w 7.8 mainshock on fault strikes ranging from 0 to 360 degrees, assuming a vertical dip (Supplementary Video S3). Calculations are performed using the best-fit static slip model of the M_w 7.8 event constrained by SAR and GNSS data (Figs. S1 and S7), and the boundary element code DIS3D (*105, 106*). Fig. S27 shows the computed perturbations in the shear, normal, and Coulomb stress (assuming the coefficient of friction of 0.6) on faults striking slightly north of west, similar to the orientation of the Çardak fault that hosted the nucleation of the M_w 7.7 event. The latter was encouraged by both the normal and shear static stress changes. Note that the Coulomb stress change is positive along a potential rupture path toward the EAF (a straight eastward continuation of the Çardak-Sürgü fault), unlike the actual rupture path along the Doğanşehir fault that experienced a decrease in the Coulomb stress (see Fig. 4D and Video S3).

Rupture velocity analysis using near-fault strong motion pulses

The SW part of the EAF is well instrumented with 16 stations located nearly on top of the fault trace. Records from these stations can thus be used to track the passage of the rupture and estimate the rupture speed. To that end, we first band-pass filter the strong motions between 0.01-1 Hz and hand-pick the onset timing of the strong pulse that marks the rupture passage. Knowing the distance between the stations, we then estimate the average rupture speed using a linear regression. We also use this approach on the ground motions predicted by our dynamic rupture model to further compare our dynamic rupture model with the observations. From the observed strong ground motions, we estimate a rupture speed of 3.25 km/s and 2.94 km/s on the EW and NS component respectively, leading to an average rupture speed of 3.10 km/s. For the modeled ground motion, we estimate an average rupture speed of 2.97 km/s (2.975 km/s on the EW component and 2.971 km/s on the NS component). This is consistent with the 2.8 km/s solution derived from our kinematic slip inversion, confirming an overall subshear rupture on the SW part of the EAF.

Ground motion analysis

We compute peak ground velocities (PGV) and peak ground accelerations (PGA) for both earthquakes from local strong motion acceleration recordings and from the dynamic rupture simulation which resolves frequencies up to 1.0 Hz in a broad region of 400×200×25 km covering the fault systems of both events and nearby strong motion stations. We compute the observed PGVs and PGAs using local strong motion data obtained from AFAD (Disaster and

Emergency Management Authority, 1973) using the automatically processed records for both the M_w 7.8 and 7.7 earthquakes. We define PGV and PGA as the rotationally-independent geometric mean (GMRotD50, *107*) of the two horizontal components of ground velocity and acceleration, respectively. We compute the Joyner-Boore distance, R_{JB} (*108*), for each station using the representation of fault rupture used in the USGS ShakeMaps (*109*).

We compute residuals from a ground motion model (*55*) developed for "all seismically-active regions bordering the Mediterranean Sea and extending to the Middle East", by taking the natural logarithm of the observational and synthetic data divided by the predictions (Fig. S23). We assume a site condition of VS30=760 m/s for the residual calculation. We used the OpenQuake (*110*) software to obtain the ground motion model predictions.

Captions for Animations

Video S1: Slip rate animation, dynamic rupture scenario of the M_w 7.8 earthquake.

Video S2: Slip rate animation, dynamic rupture scenario of the M_w 7.7 earthquake.

Video S3: Static stress changes due to the M_w 7.8 earthquake on vertical strike-slip faults, as a function of strike angle, at depth of 5 km.

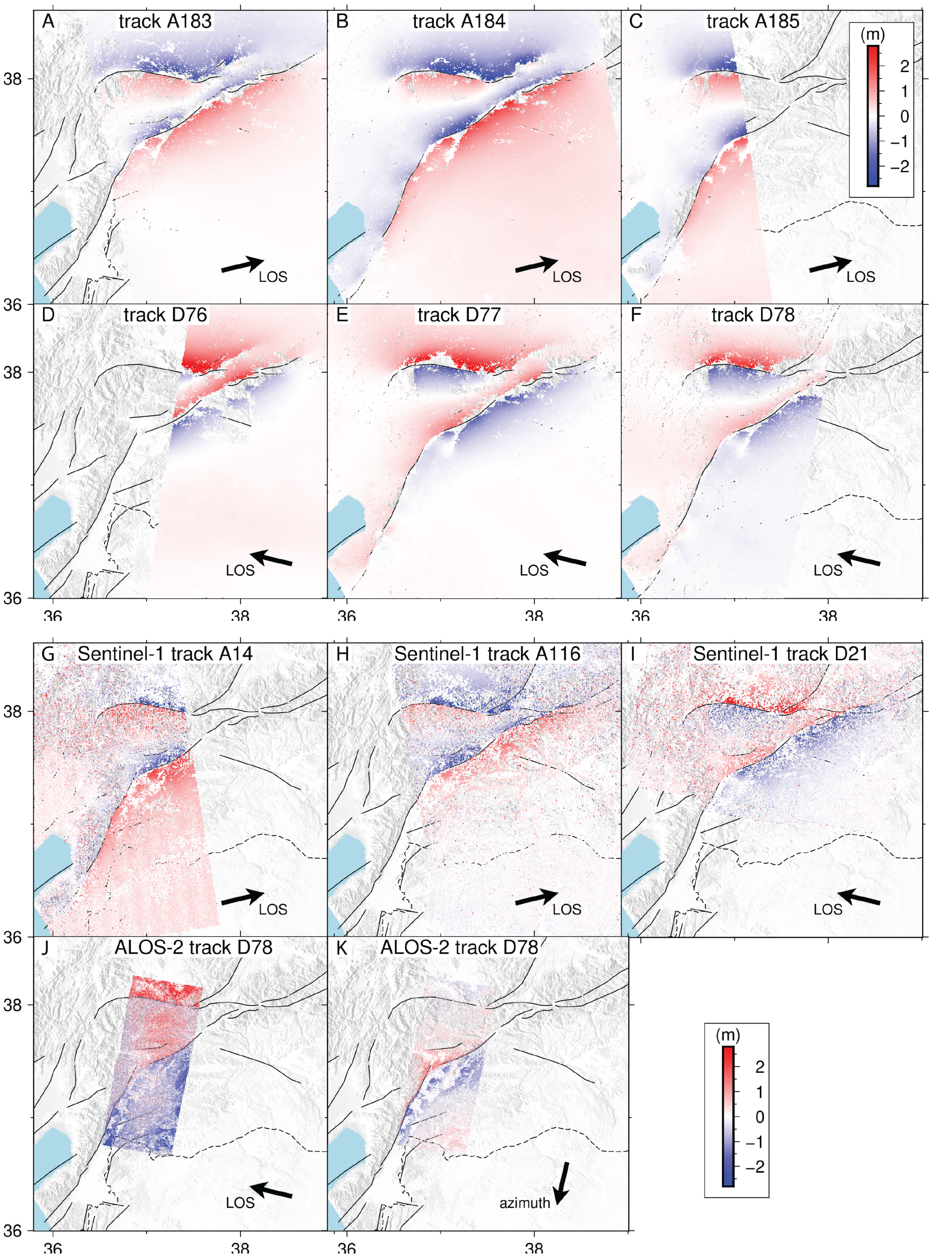

Fig. S1. Line of sight (LOS) displacements and pixel offsets used in this study. (a-f) LOS displacements from ALOS-2 ScanSAR interferograms from ascending tracks 183, 184, and 185, and descending tracks 76, 77, and 78. (g-jb) Range and (k) azimuth offsets derived from the TOPS SAR data from Sentinel-1 tracks A14, A116, D21 (g-i), and stripmap mode data from ALOS-2 descending track D78 (j,k). Horizontal and vertical axes represent longitude and latitude, in degrees. Colors represent displacement amplitude, in meters. Arrows denote a line of sight from the radar antenna to the ground, and a positive direction of the LOS displacements and azimuth offsets.

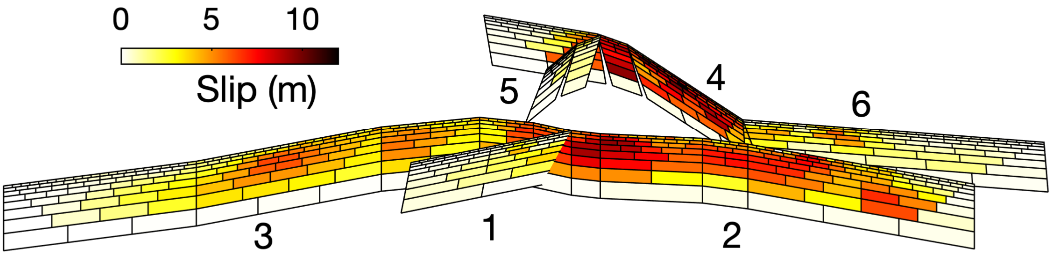

Fig. S2. Static slip distribution from inversions of space geodetic (SAR and GNSS) data, from a different perspective than in Fig. 1B, showing the slip distribution on fault segments 1 and 3 in greater detail. Notation is the same as in Fig. 1B.

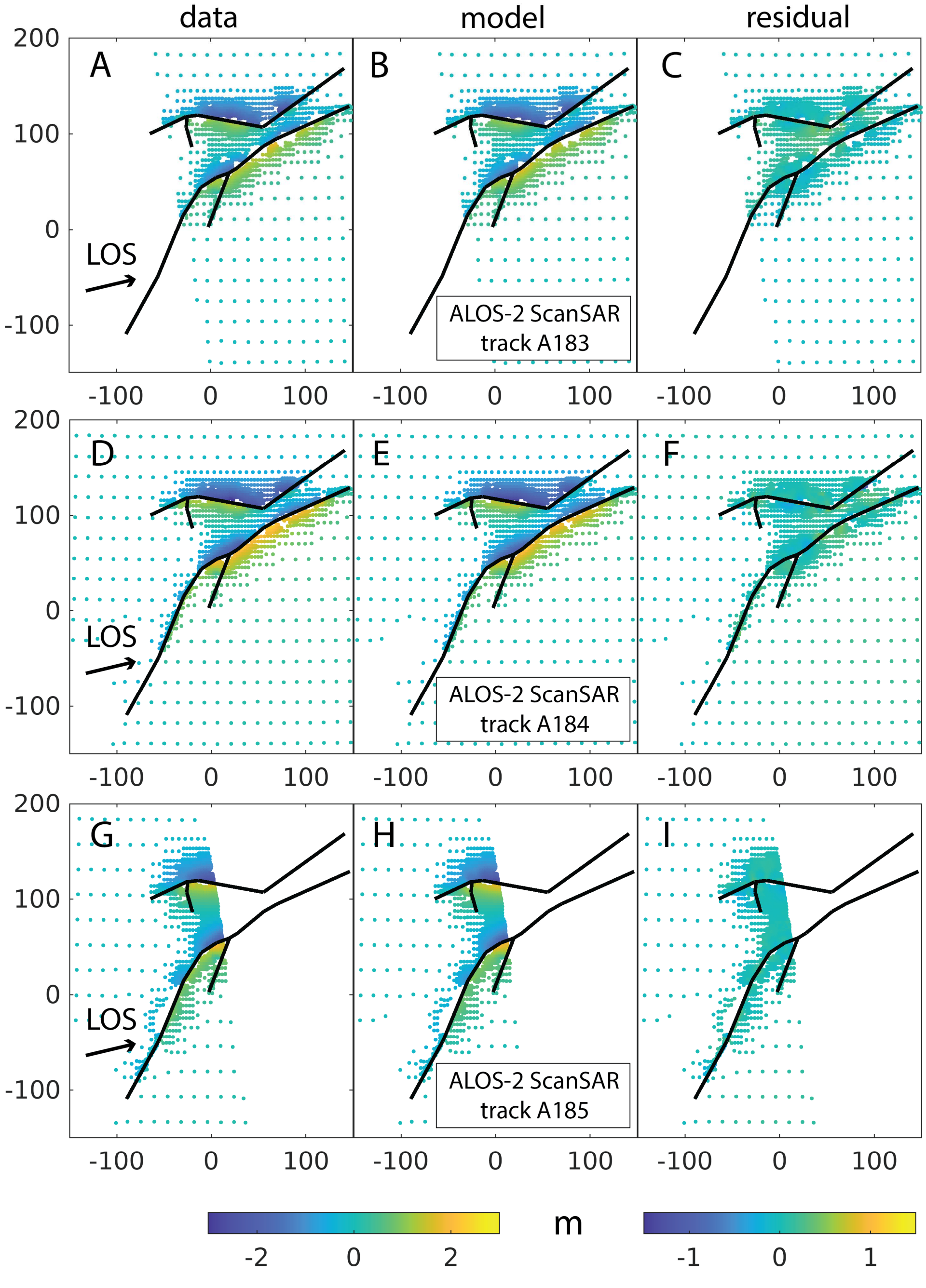

Fig. S3.
Sub-sampled data, model predictions and residuals for the ALOS-2 ScanSAR interferograms from the ascending tracks 183 (a-c), 184 (d-f), and 185 (g-i). Horizontal and vertical axes represent eastings and northings in local UTM coordinates, in kilometers, with origin at 37°E, 37°N. Colors represent displacements, in meters.

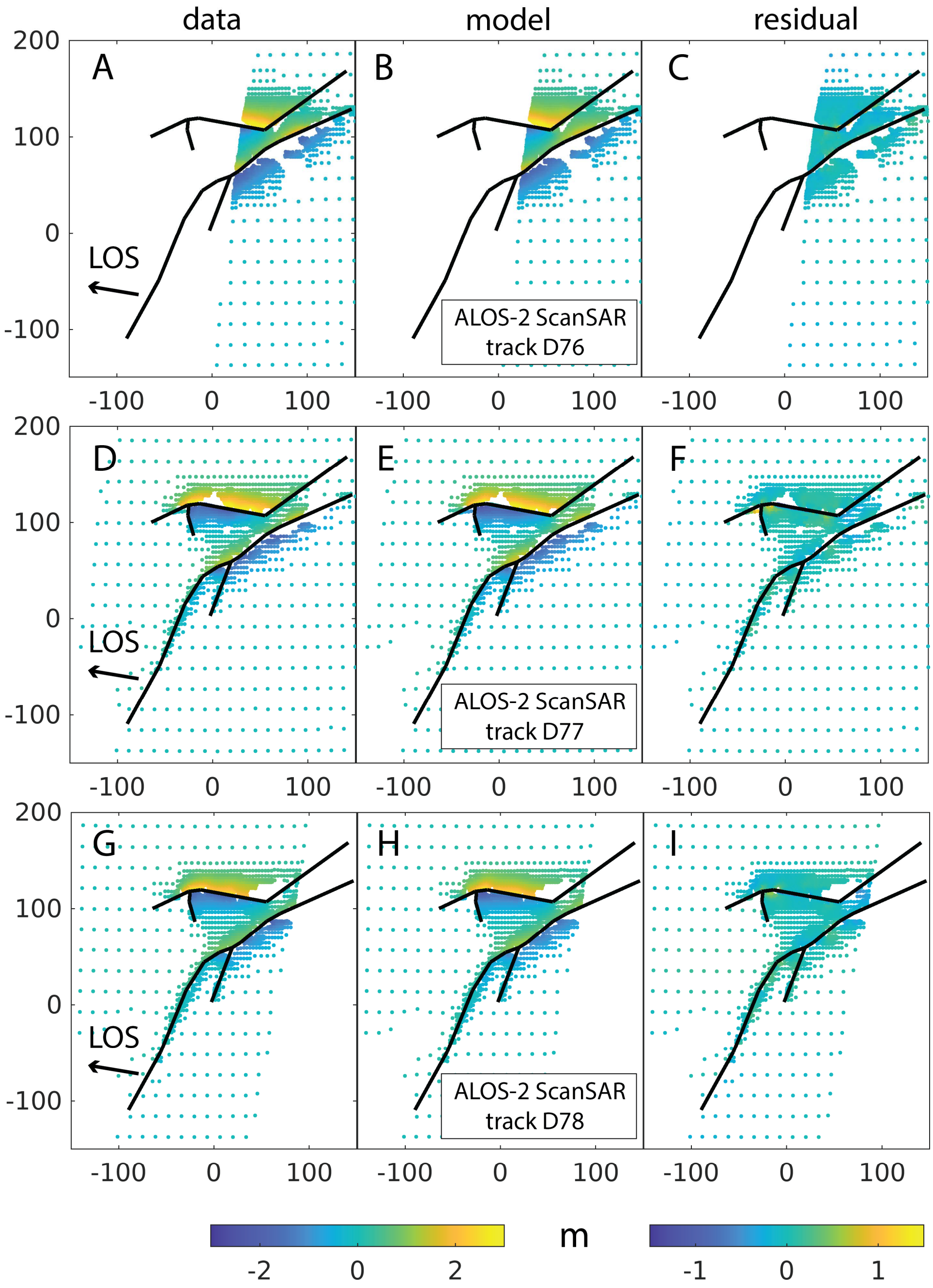

Fig. S4.

Sub-sampled data, model predictions and residuals for the ALOS-2 ScanSAR interferograms from the descending tracks 76 (a-c), 77 (d-f), and 78 (g-i). Horizontal and vertical axes represent eastings and northings in local UTM coordinates, in kilometers, with origin at 37°E, 37°N. Colors represent displacements, in meters.

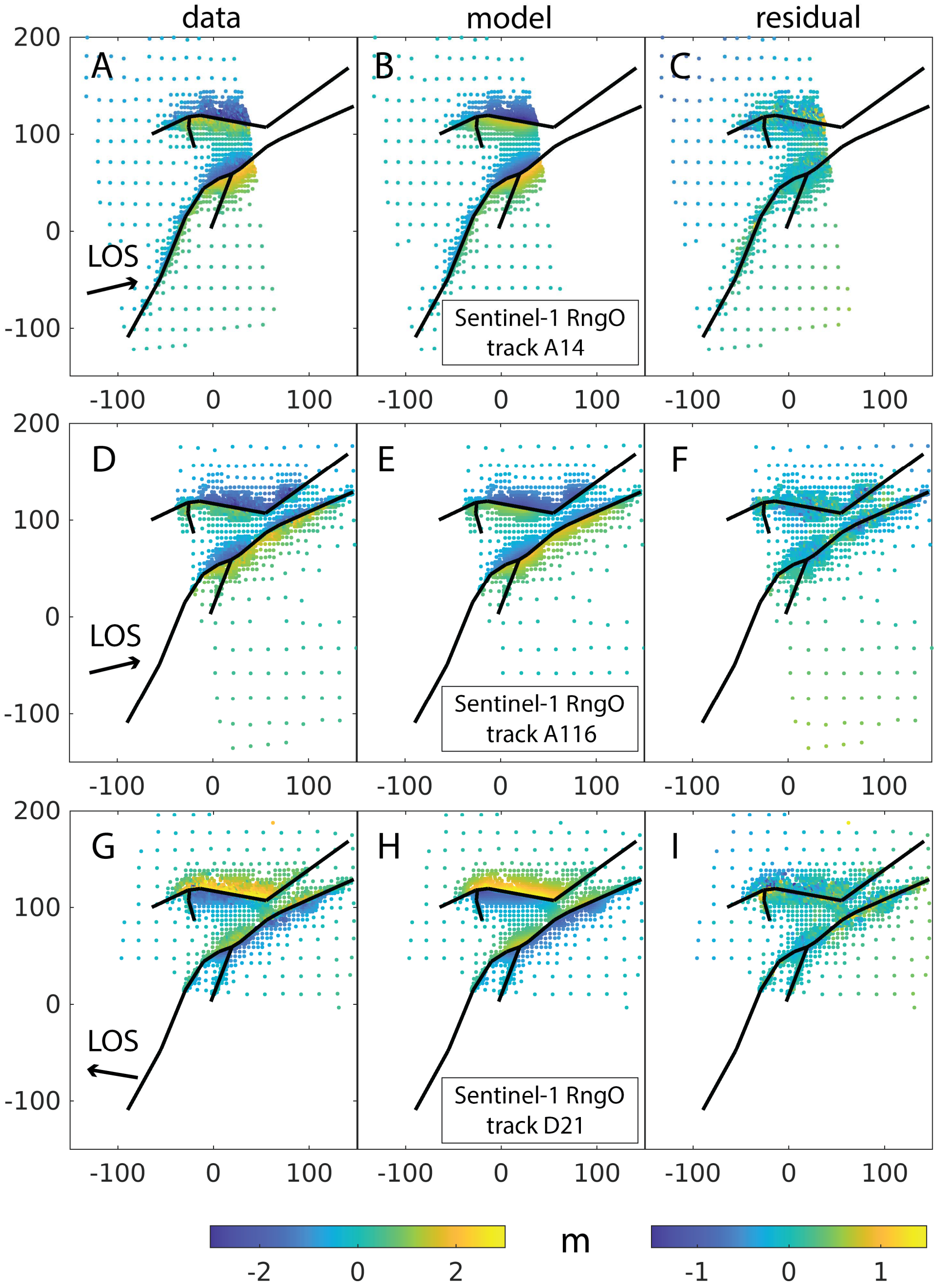

Fig. S5.

Sub-sampled data, model predictions and residuals for the Sentinel-1 range offsets from the ascending tracks 14 (a-c), 116 (d-f), and descending track 21 (g-i). Horizontal and vertical axes represent eastings and northings in local UTM coordinates, in kilometers. Colors represent displacements, in meters.

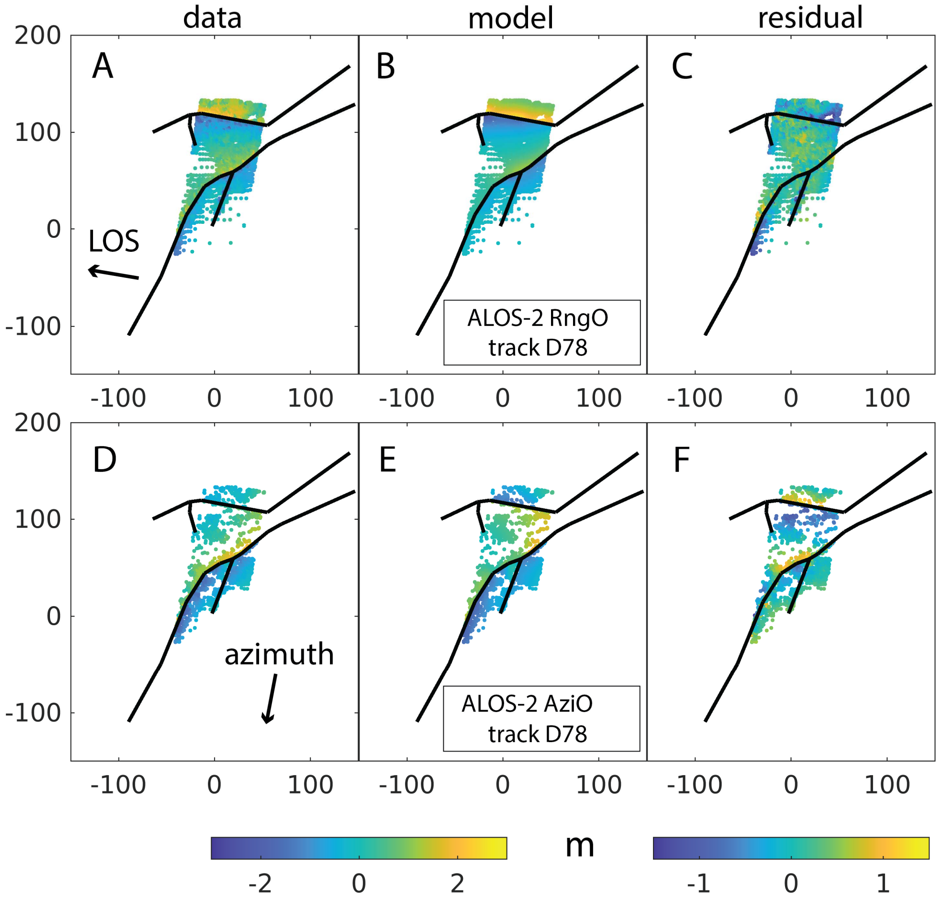

Fig. S6.

Sub-sampled data, model predictions and residuals for the ALOS-2 range offset (a-c) and azimuthal offset (d-f) from descending track 78. Horizontal and vertical axes represent eastings and northings in local UTM coordinates, in kilometers. Colors represent displacements, in meters.

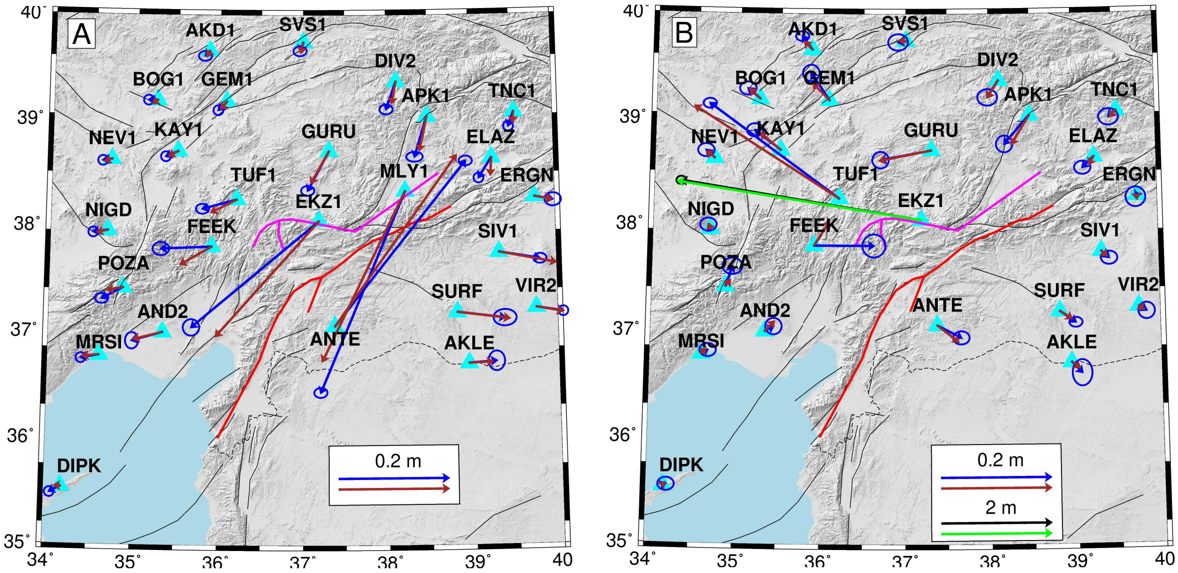

Fig. S7.

Comparison between GNSS observations (blue arrows) and model predictions (dark red arrows) from the M_w 7.8 event (a) and the M_w 7.7 event (b). In panel (b), black and green arrows represent the observed and modeled displacements at site EKZ1, which are substantially larger than displacements at all other sites, thus shown on a different scale. Ellipses denote 2-sigma errors in the displacement solutions.

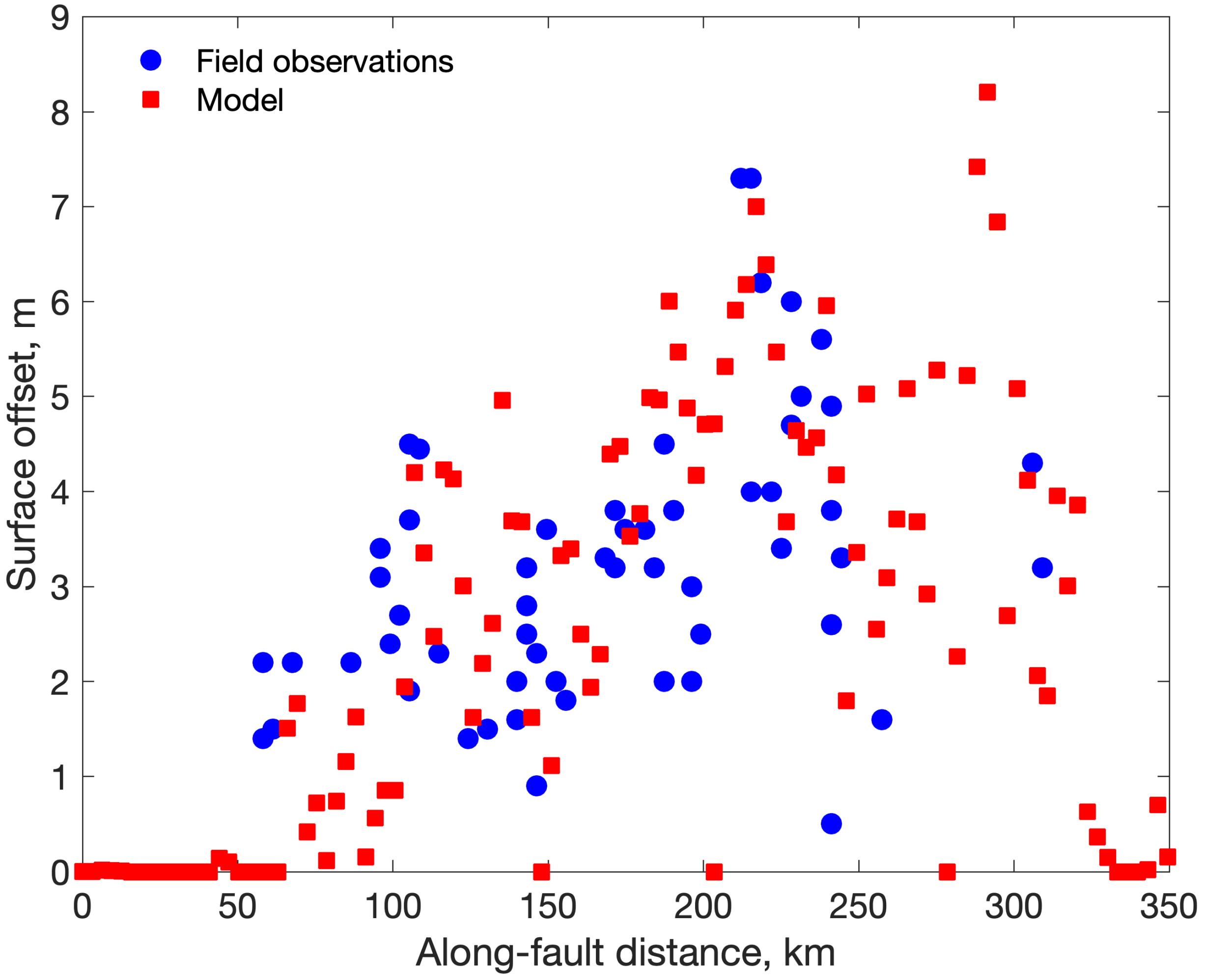

Fig. S8.

Comparison between the surface slip predicted by our preferred static slip model (Fig. S2) and geologically mapped surface offsets (*18*) for the M_w 7.8 event. The along-fault profile starts at the southwestern tip of our slip model (Fig. 1B). Note that the field observations shown in this figure were not used to constrain our models. Both the model and the data suggest a considerable heterogeneity in slip amplitude along the earthquake rupture.

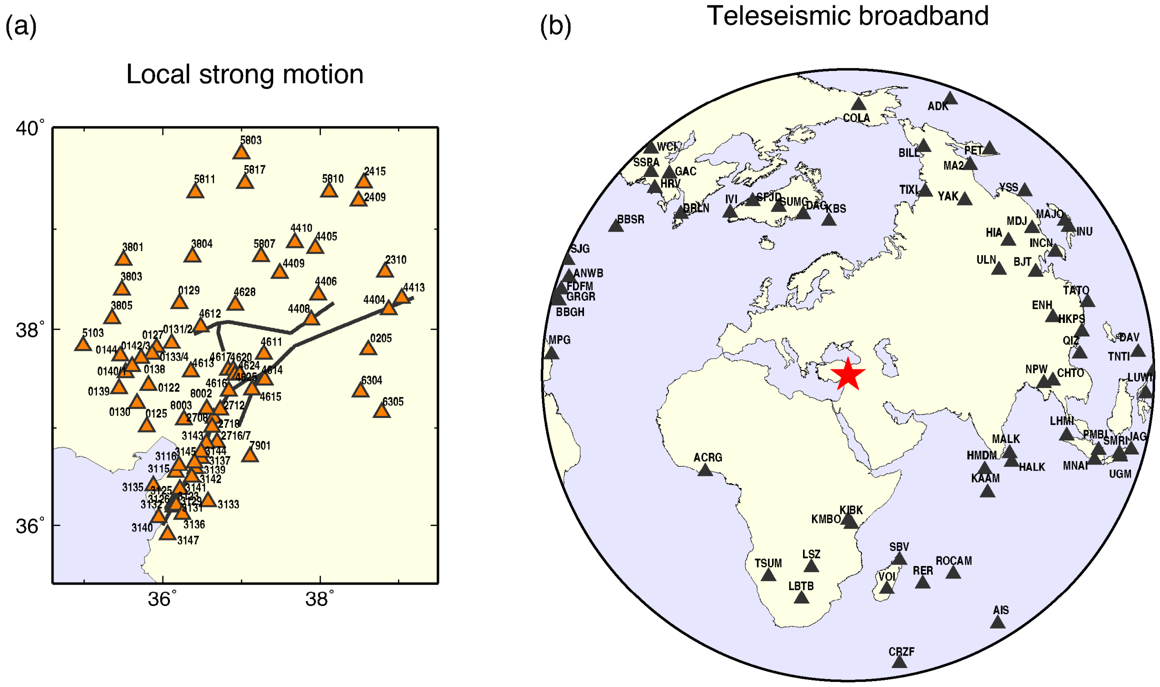

Fig. S9.

Seismic stations (triangles) used in the subevent and kinematic finite-fault inversions. Strong motion stations are in orange, and teleseismic stations are in black.

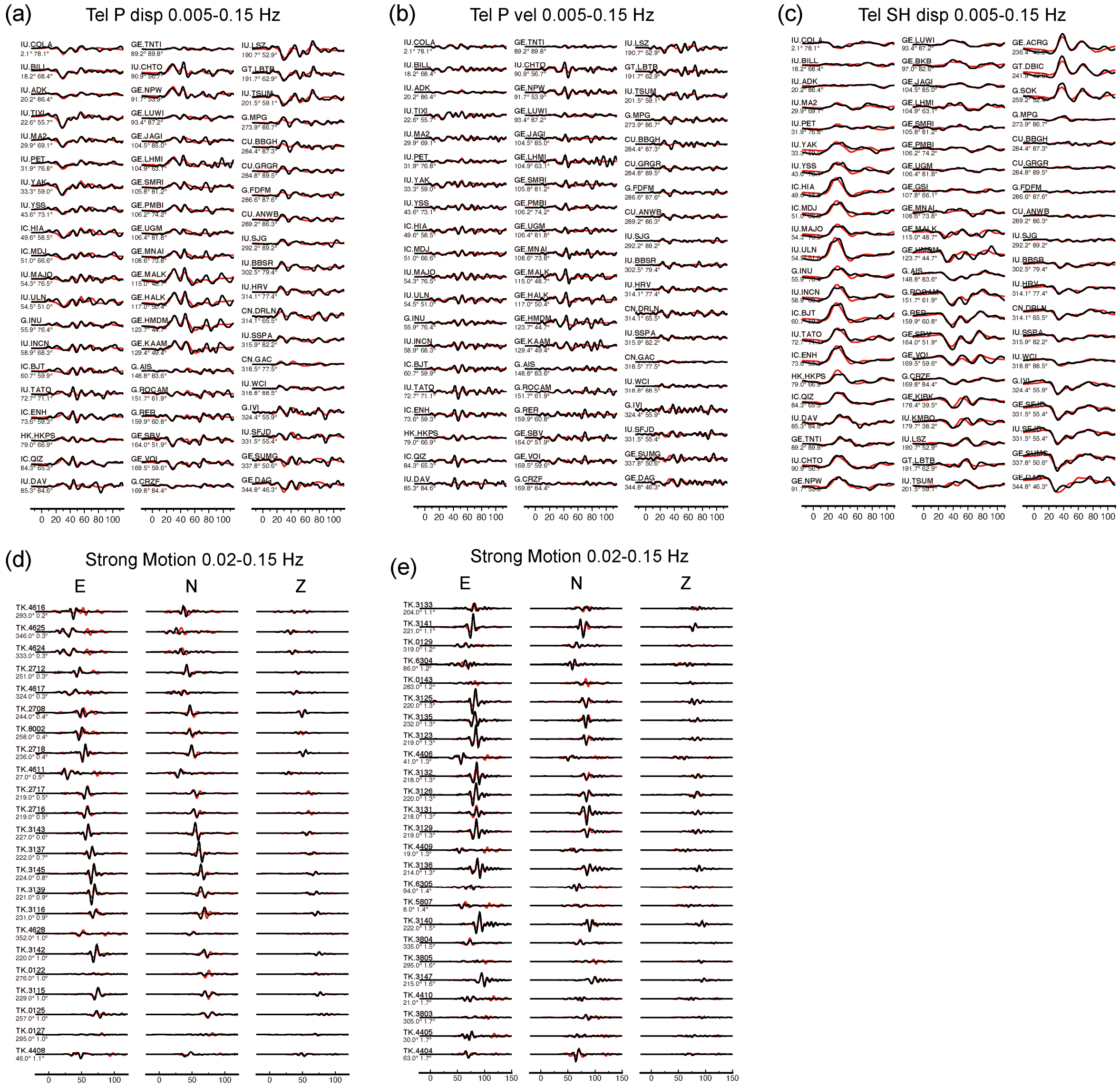

Fig. S10.

Waveform fits of the preferred subevent model for the M_w 7.8 event. Observed data and synthetics are indicated by black and red lines, respectively. The numbers leading each trace are the station azimuth and distance. (a) P waves in displacement. (b) P waves in velocity. (c) SH waves in displacement. (d-e) Local full strong motion waveforms in velocity.

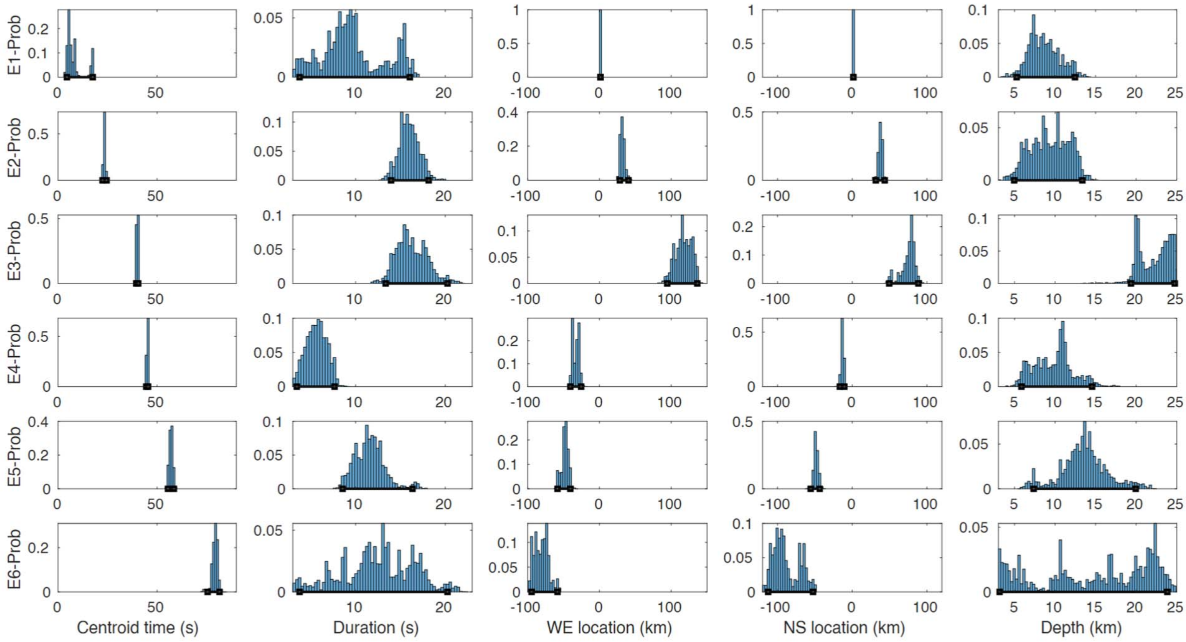

Fig. S11.

Subevent model uncertainties from the Markov Chain sample distributions. Columns from left to right indicate the density distribution of subevent centroid times, durations, west-east locations, north-south locations and centroid depths. Rows represent subevents E1-E6.

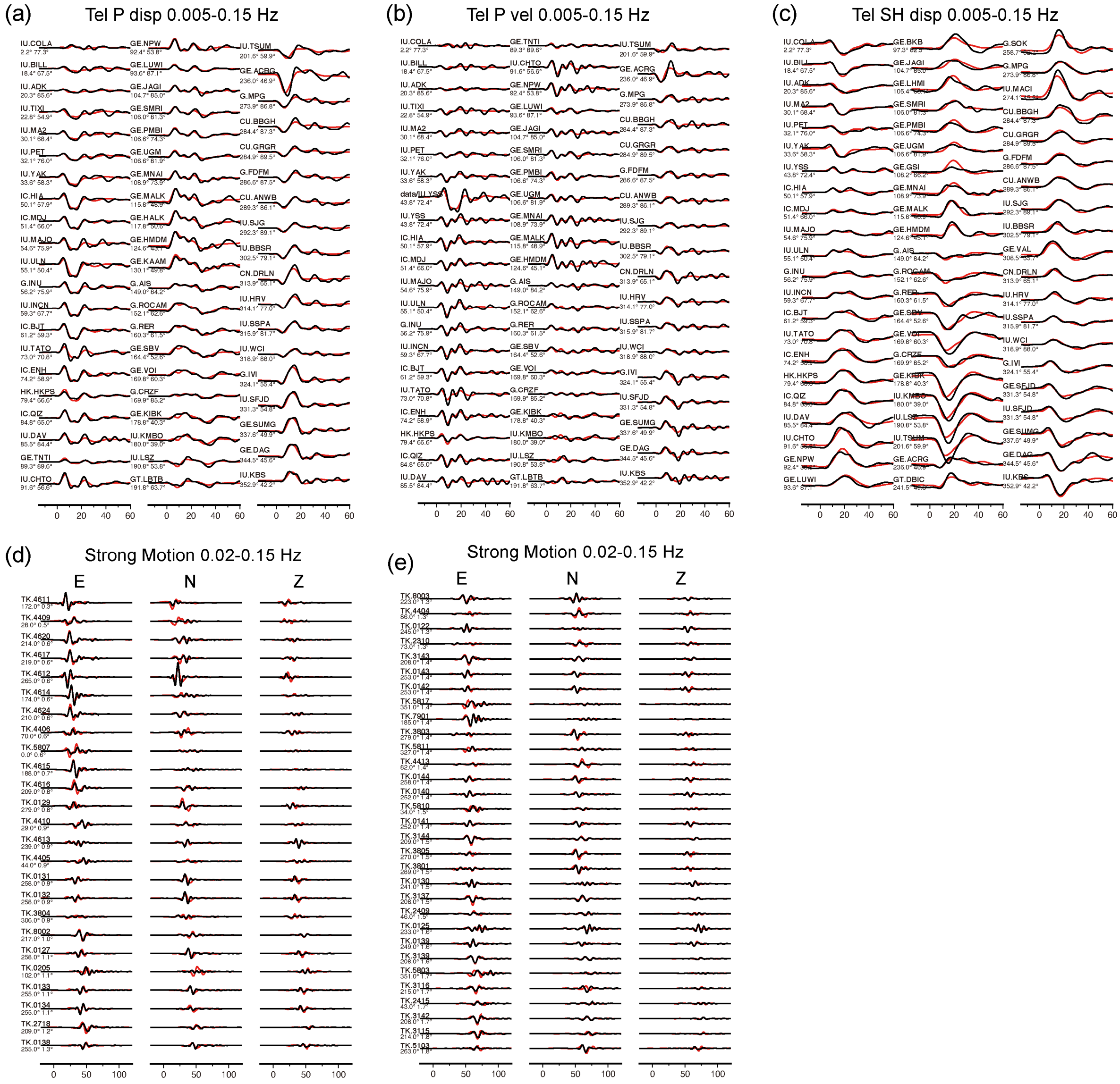

Fig. S12.

Similar to Fig. S10 but for the M_w 7.7 event.

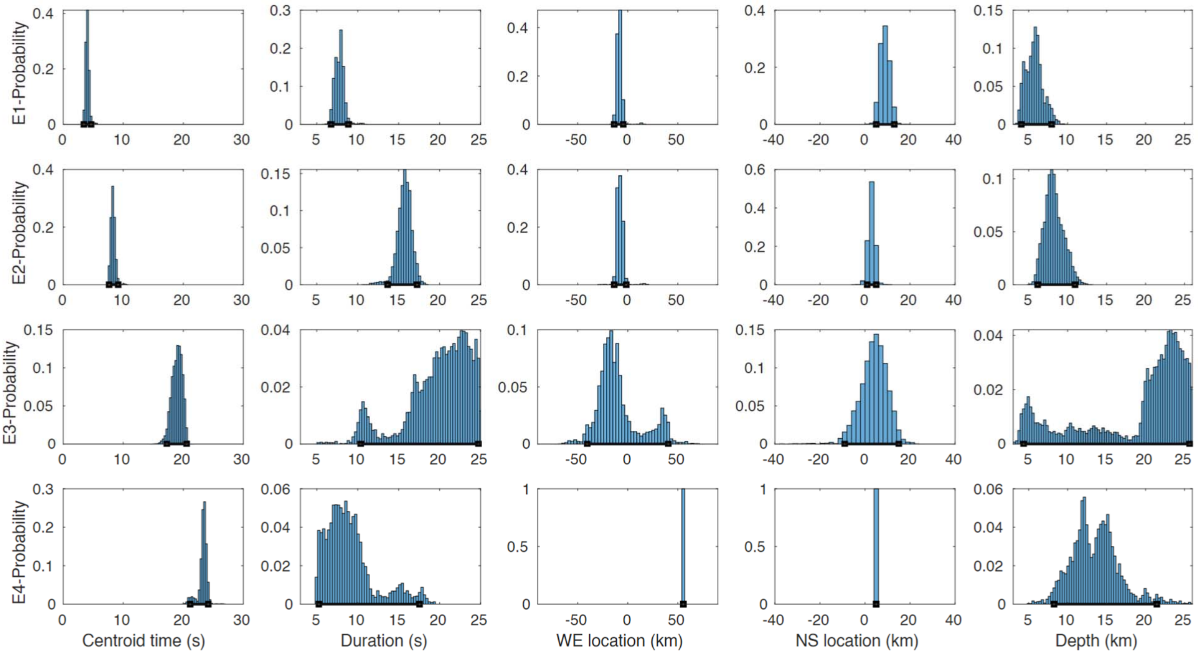

Fig. S13.
Similar to Fig. S11 but for the M_w 7.7 event.

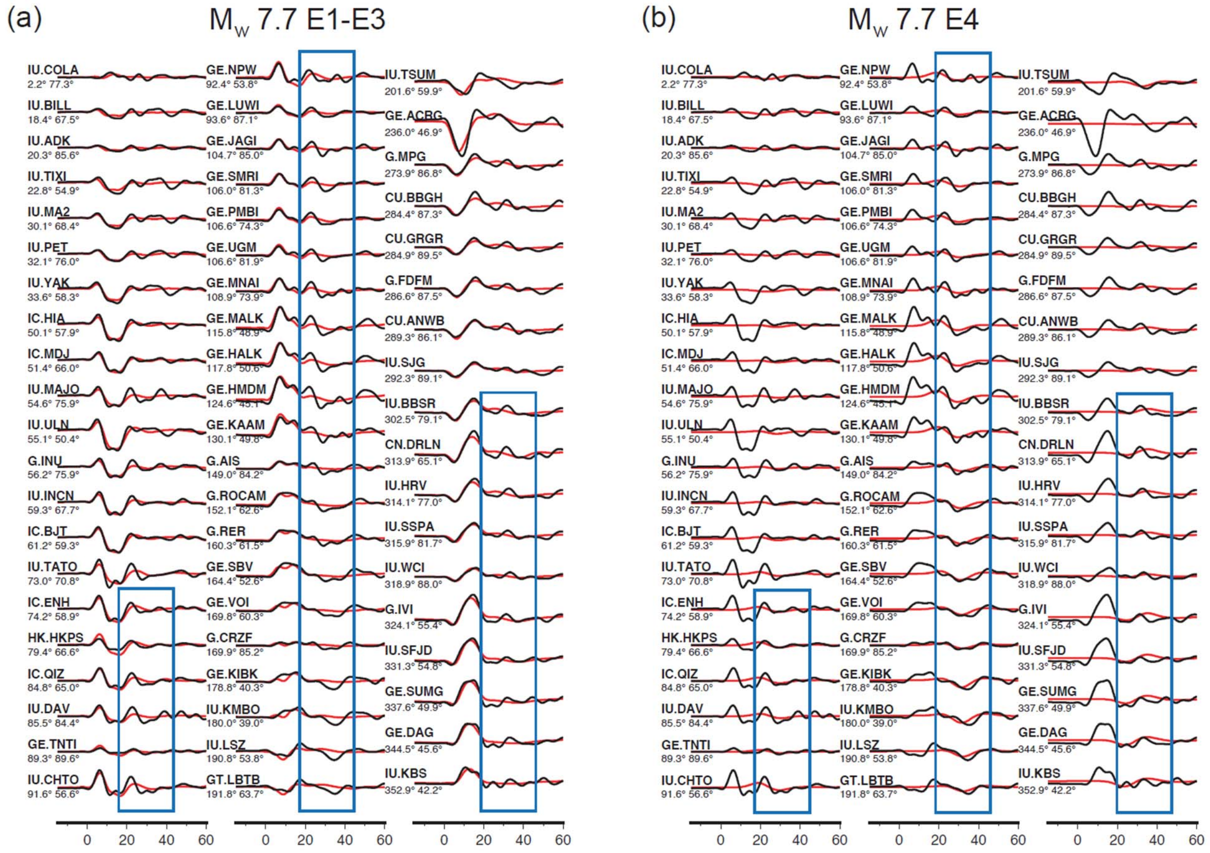

Fig. S14.
Contributions to the teleseismic P waves in displacement from (a) subevents E1-E3 and (b) subevent E4 for the *M_w* 7.7 earthquake. The boxed areas show that the seismic data fits require contribution from E4.

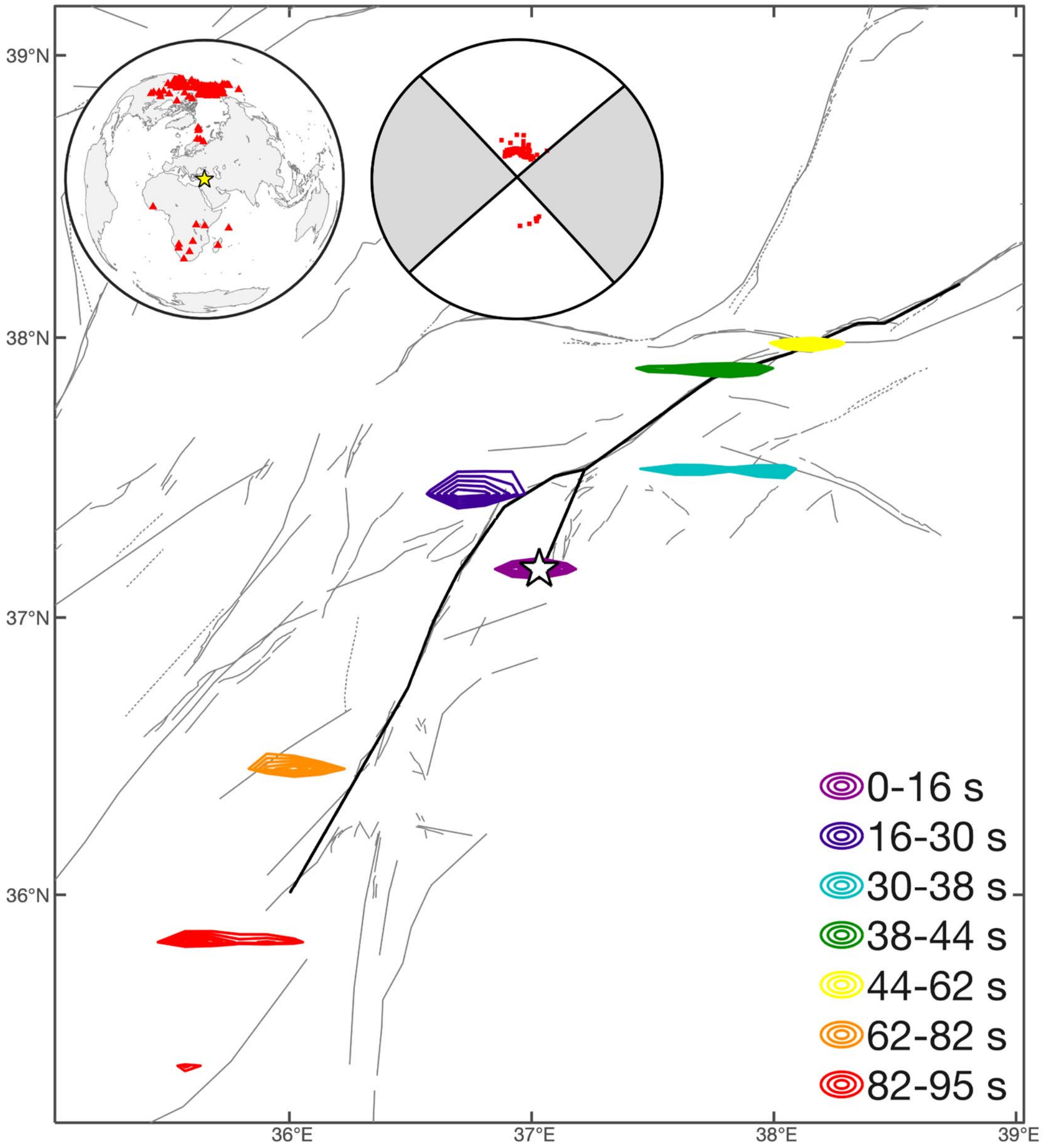

Fig. S15.
Back-projection results for the M_w 7.8 earthquake. Color contours indicate the normalized peak energy radiation for specific time windows. Insets display the stations utilized for the analysis and their corresponding P wave polarity in the lower-hemisphere projection.

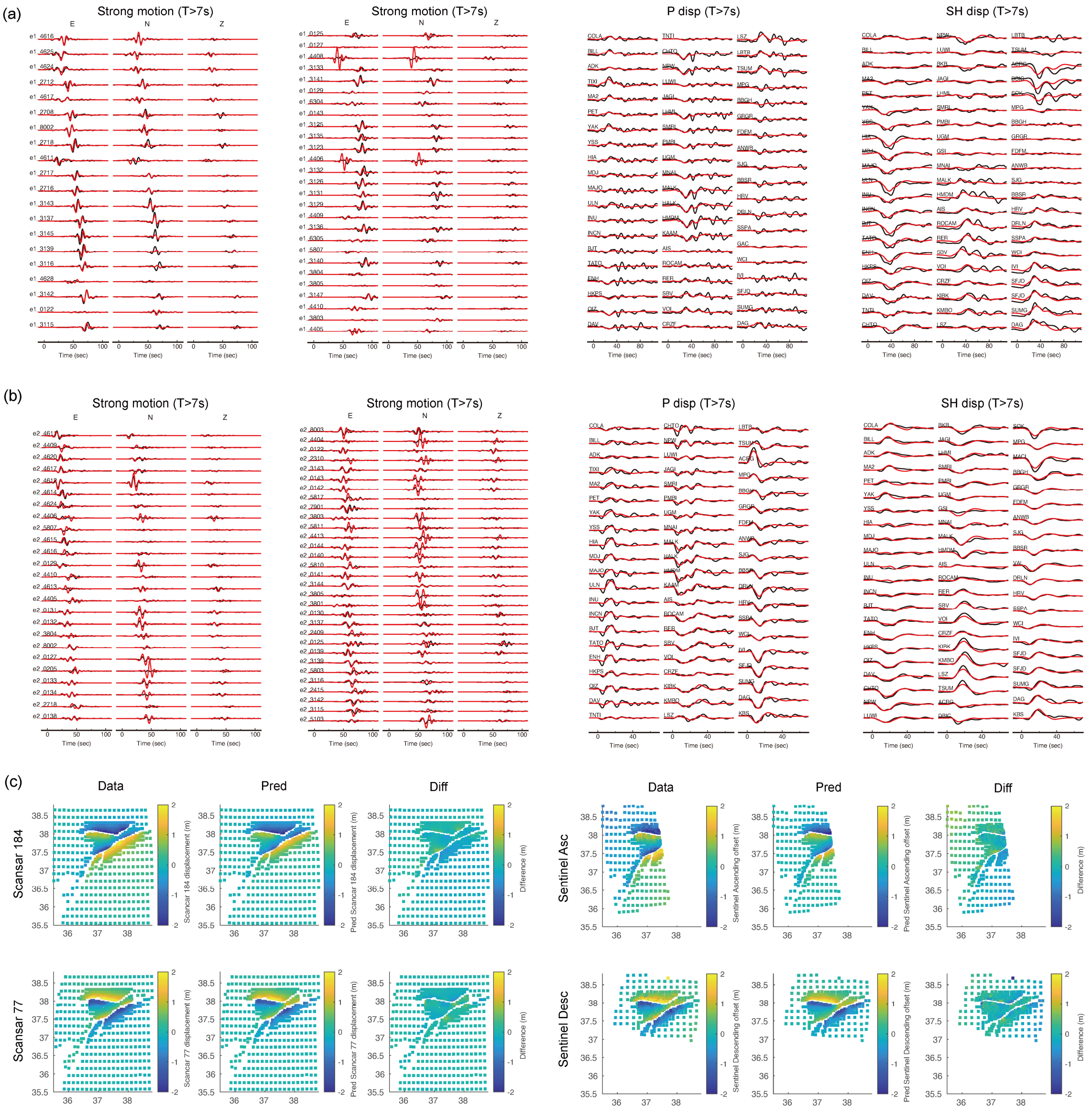

Fig. S16.

Data fits of the kinematic finite-fault model. (a) Fits to the near- and far-field seismic waveforms for the M_w 7.8 earthquake. (b) same as (a) but for the M_w 7.7 event. (c) Comparison of data and predictions of line-of-sight displacements for the Scansar track 184 and 77, and range offsets for the Sentinel ascending and descending tracks.

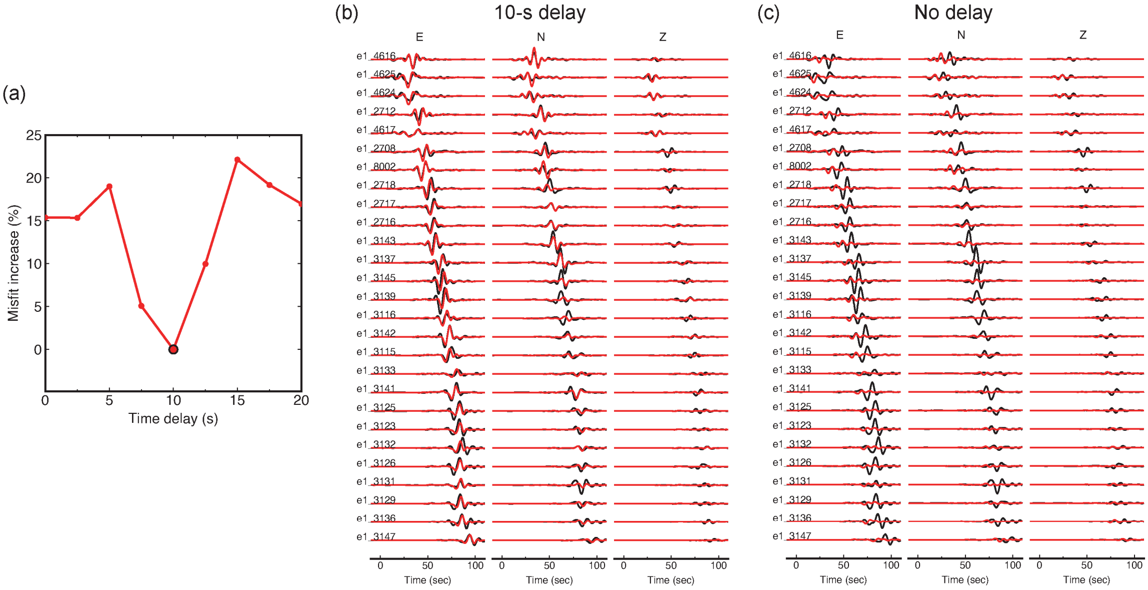

Fig. S17.
Delay of the backward branching along the southwest segment of the EAF during the M_w 7.8 earthquake. (a) Optimal delay of 10 s constrained by grid-search. (b) Fits to the on-fault strong-motion waves with 10-s time delay. (c) Fits to the on-fault strong motion waves without time delay.

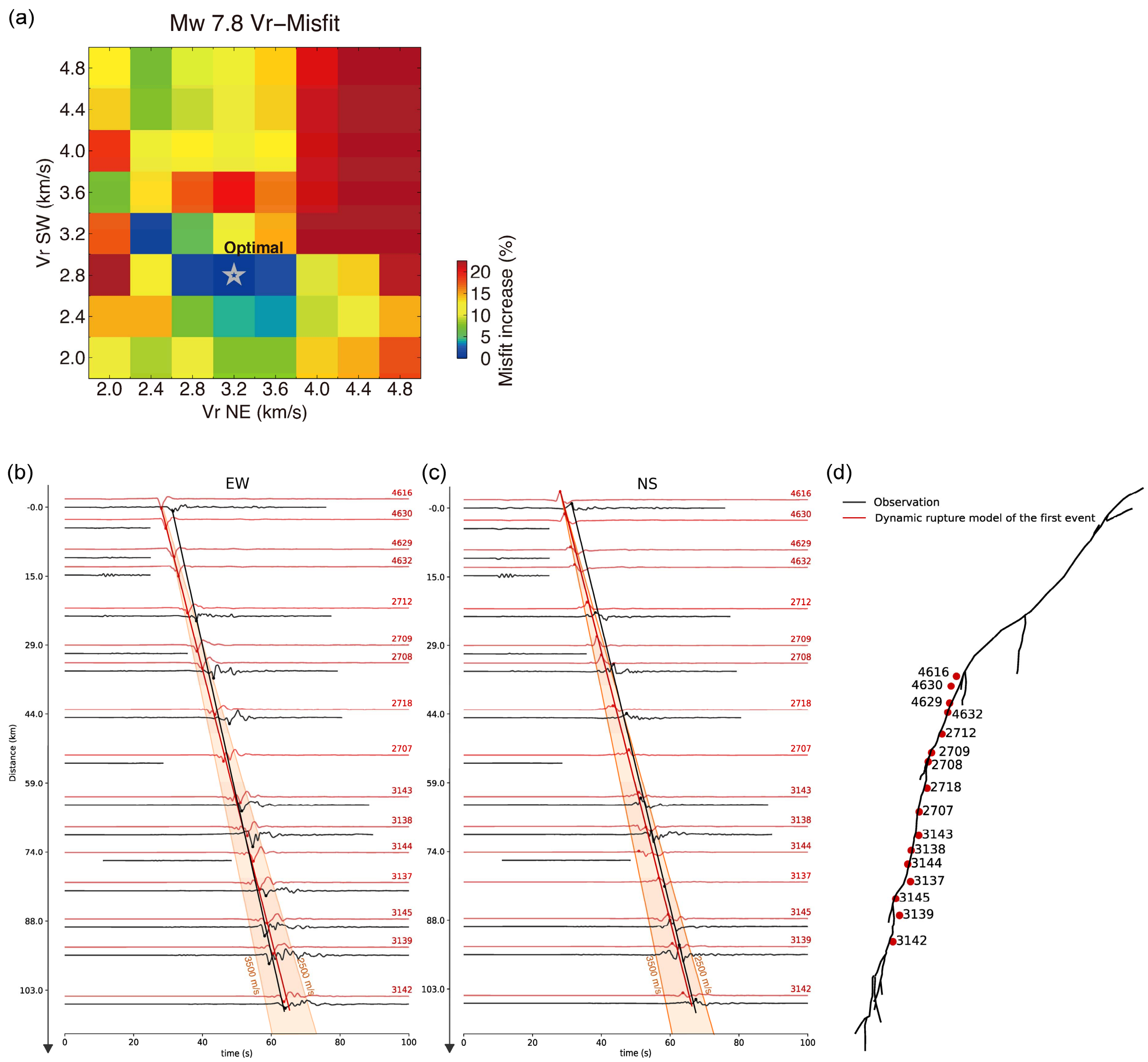

Fig. S18.
Rupture velocity analysis for the M_w 7.8 earthquake. (a) Data misfits of the kinematic slip inversion as a function of rupture velocities towards northeast and southwest directions, respectively. (b) Estimates of average rupture speed on the southwestern part of the East Anatolian Fault (EAF), using EW/NS components of the observed (black) and dynamic rupture synthetic (red) ground motions for the stations located atop the SW-EAF. For each station, the observed and modeled ground motions are offset for visibility. We use the respective peak of the first strong velocity pulse, marked by black and red points, in each waveform to estimate the rupture speed. The black and red straight lines are the resulting estimated average rupture speeds.

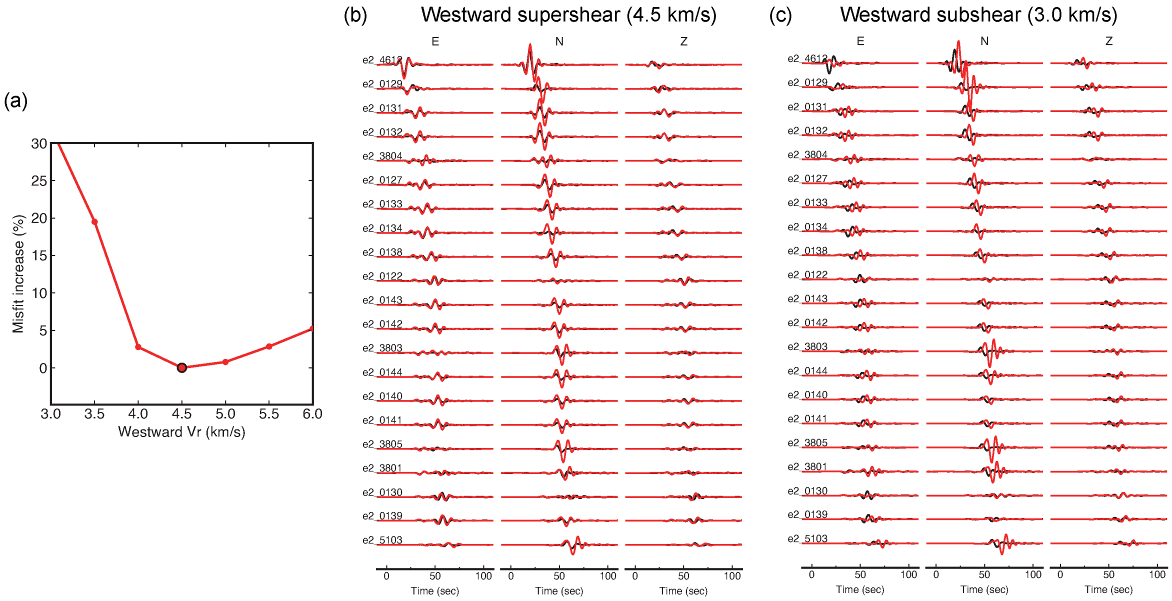

Fig. S19.

Westward supershear rupture velocity during the M_w 7.7 earthquake. (a) Optimal westward rupture velocity of 4.5 km/s constrained by grid-search. (b) Fits to the west-propagating strong-motion waves with a supershear rupture velocity of 4.5 km/s. (c) Fits to the west-propagating strong motion waves with a subshear rupture velocity of 3.0 km/s.

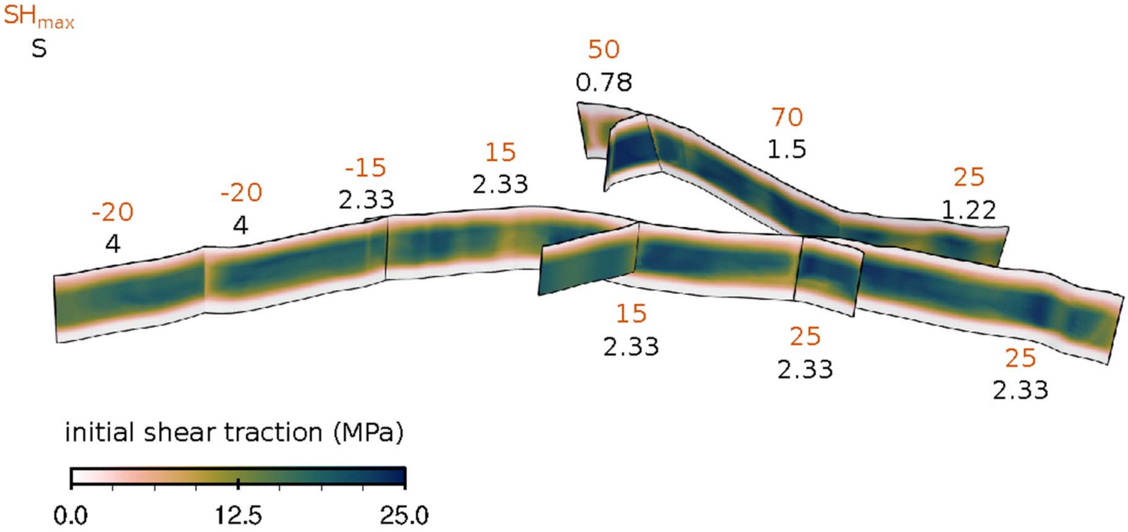

Fig. S20.
Initial conditions for dynamic rupture modeling of both large earthquakes. *SHmax* (orange numbers) is the complex regional maximum horizontal compressional stress loading on all faults and varies across the fault system. *S* (black numbers) is the ratio of initial strength excess to nominal stress drop and a measure of the relative strength of each fault segment (*84*). Additional small-scale initial shear-stress heterogeneity is constrained from the static slip model (Fig. 1).

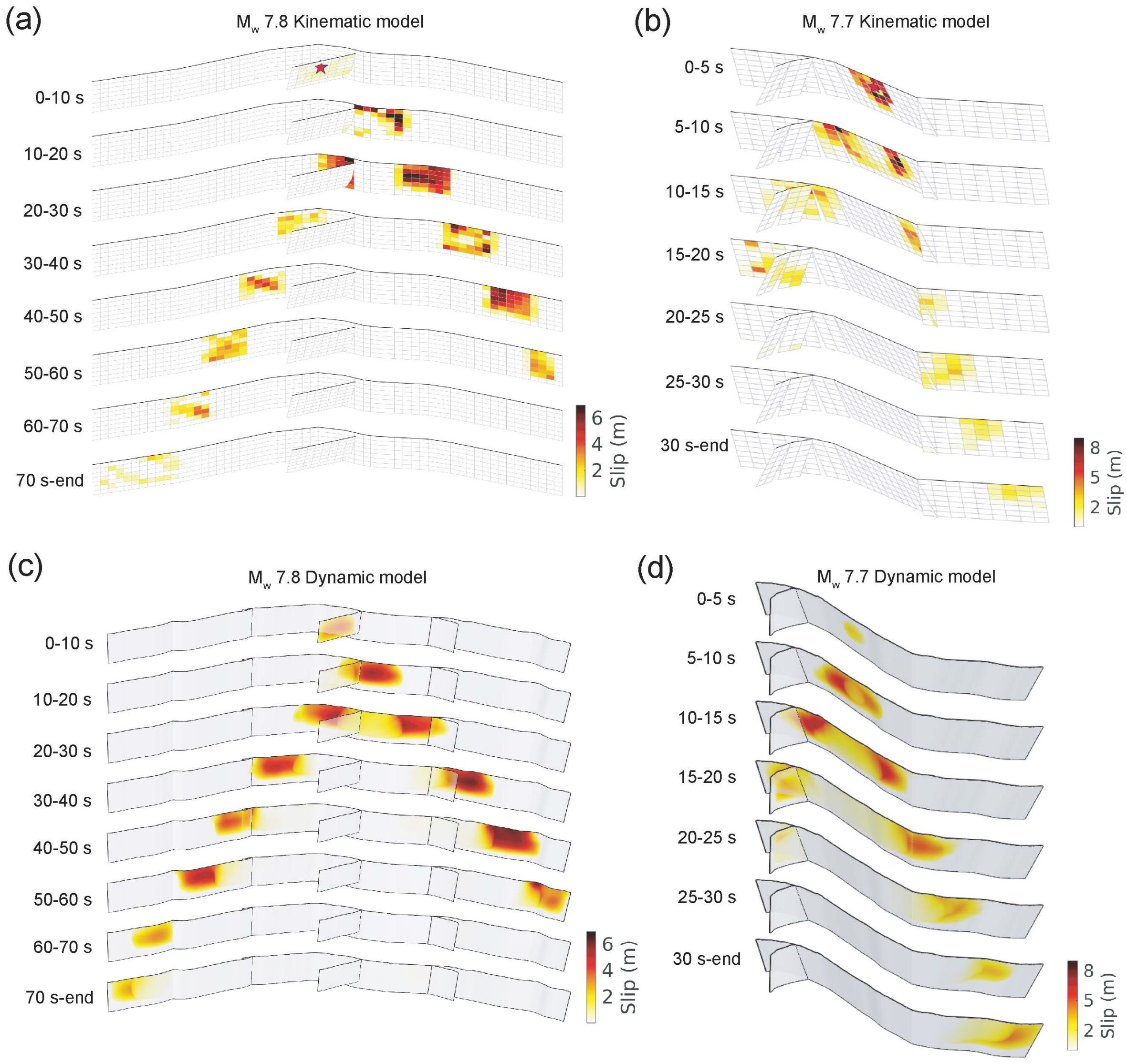

Fig. S21.
Comparison of the accumulated slip at different time intervals from kinematic slip models for the (a) M_w 7.8 and (b) M_w 7.7 earthquakes, with dynamic models for the (c) M_w 7.8 and (d) M_w 7.7 earthquakes, respectively.

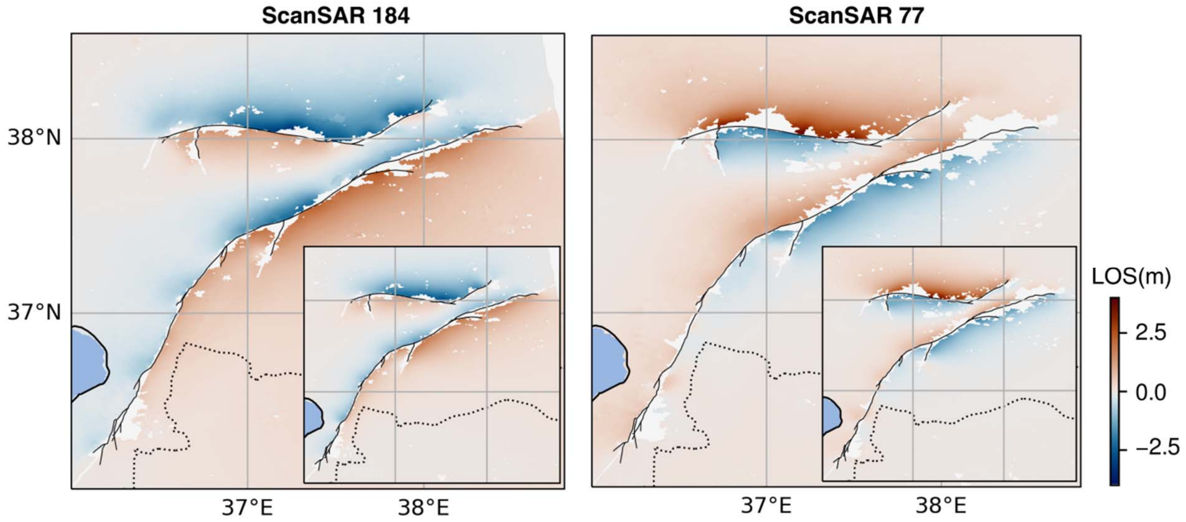

Fig. S22.
Comparison of the surface displacements predicted by our dynamic rupture models (inset) with the interferograms derived from ScanSAR data from ALOS-2 ascending track 184 (left) and descending track 77 (right). RMS mismatch between InSAR data and predictions is 0.14 m and 0.12 m for track 184 and 77, respectively.

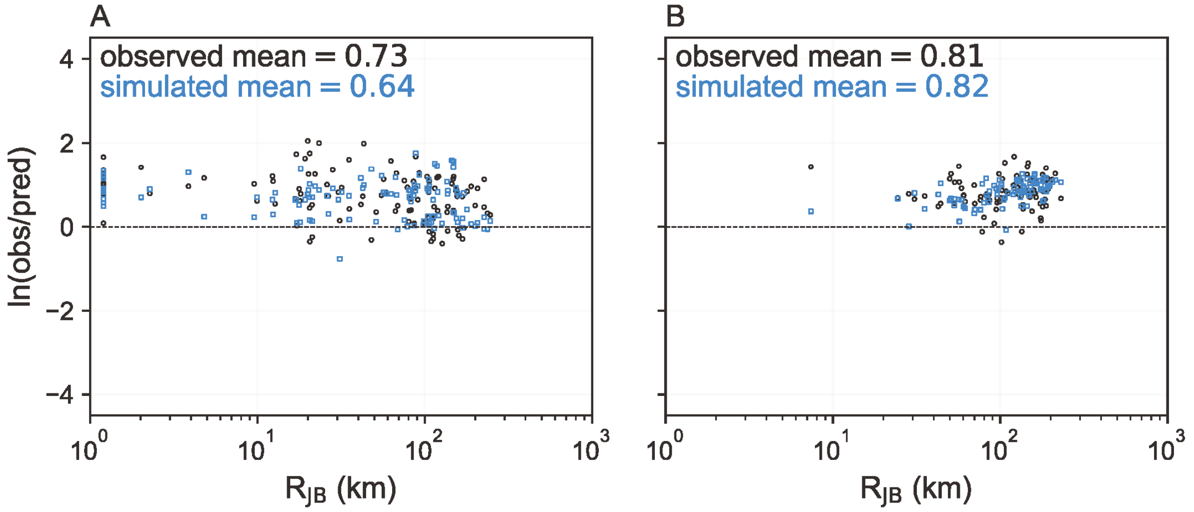

Fig. S23.
GMPE (55) residuals for the observed and simulated peak ground velocities (PGV) plotted against Joyner-Boore distance (RJB) for the (a) M_w 7.8 and (b) M_w 7.7 earthquakes of Fig. 5 of the main text. All PGV are rotationally-independent geometric mean values (GMRotD50, *107*). The residuals for the observed PGVs are shown by open black circles, and the residuals for the dynamic-rupture-simulated PGVs are shown by open blue squares. We bin the residuals by RJB and indicate the medians for each distance bin with solid markers. The means of the residuals are printed in the upper left of each panel. We include simulated and observed data at the same locations, respectively.

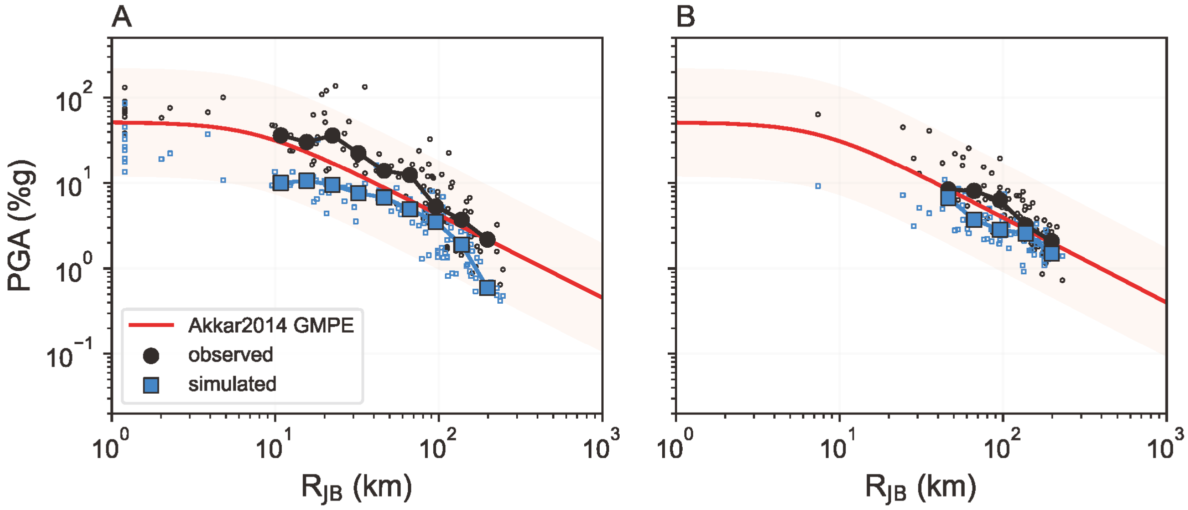

Fig. S24.
Similar to Fig. 5 but comparing peak ground accelerations (PGA) plotted against Joyner-Boore distance (R_{JB}) for the (a) M_w 7.8 and (b) M_w 7.7 earthquakes. Modeled and observed PGAs, which are more sensitive to high frequency radiation than PGVs, agree to first order. Observed PGAs from strong motion accelerometers are indicated by open black circles, and simulated PGAs from the dynamic rupture simulations are indicated by open blue squares. All PGA are rotationally-independent geometric mean values (GMRotD50). We bin the PGA data and synthetics by R_{JB} and plot the medians for each distance bin (solid markers). We include simulated and observed data at the same locations, respectively.

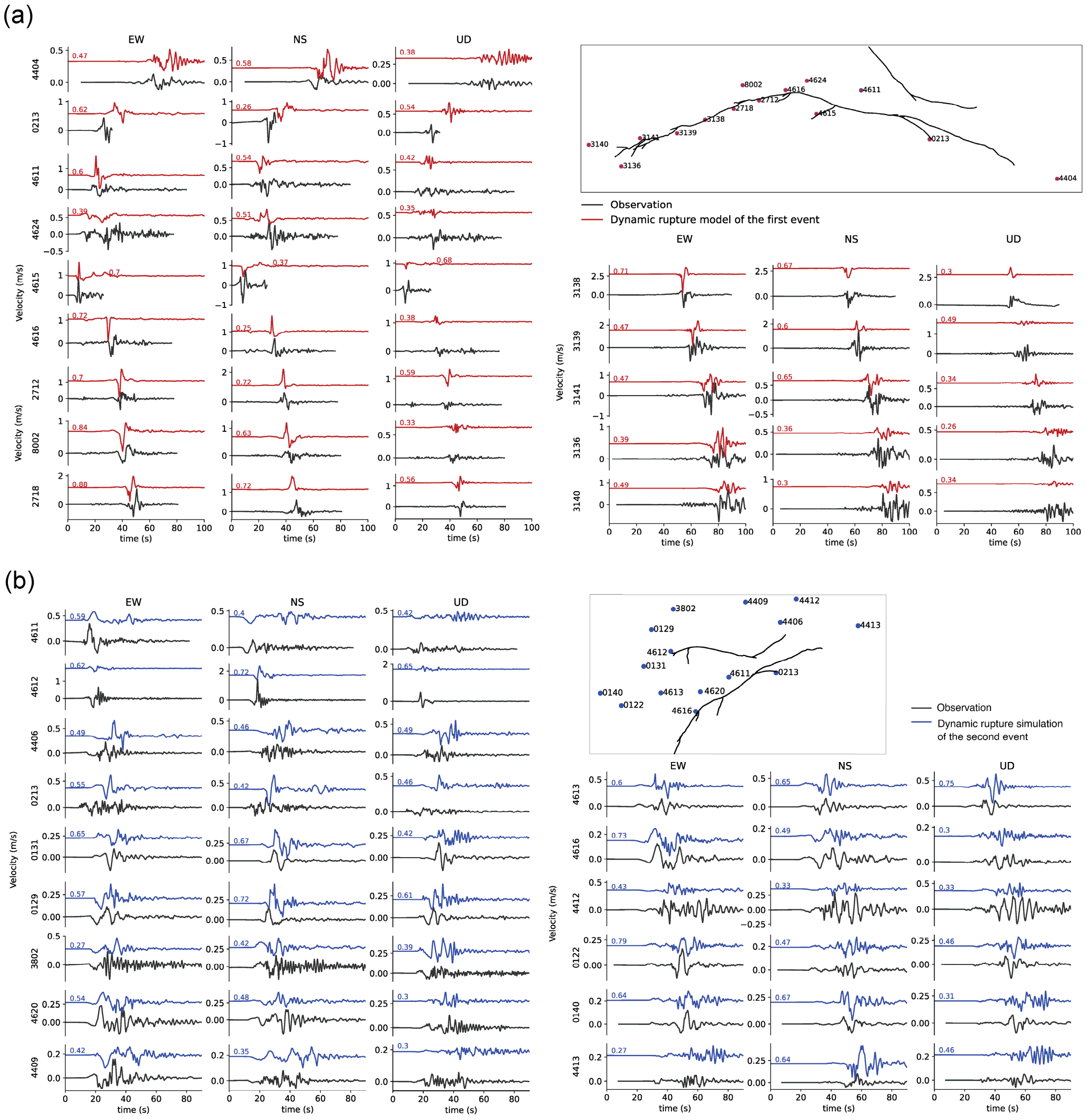

Fig. S25

Comparison for the dynamic rupture scenario of modeled (red/blue) and observed strong ground motions (black) for (a) the M_w 7.8 and (b) the M_w 7.7 earthquakes, respectively. Ground velocity time series at near-fault strong-motion stations are band-pass filtered between 0.01-1 Hz. No amplitude scaling or time shifts are applied.

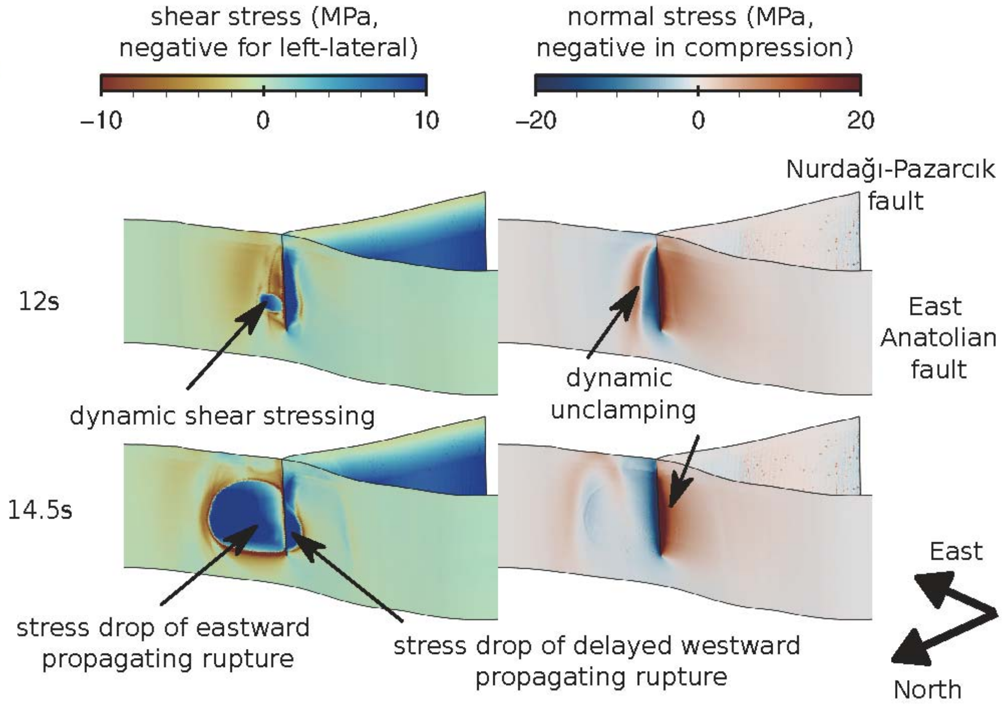

Fig. S26.
Transient shear stressing (left) and dynamic unclamping (right) effects at the fault intersection due to the northeastward rupture along the EAF.

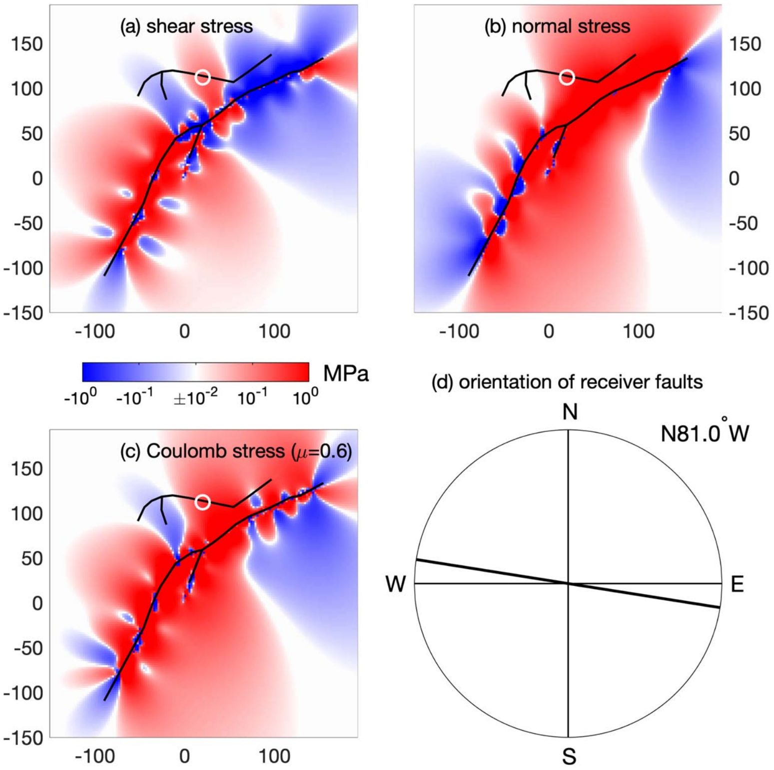

Fig. S27.
Static stress changes due to the M_w 7.8 mainshock, resolved on vertical faults striking 279 degrees (81 degrees counterclockwise from north), similar to the strike of the Çardak fault near the nucleation site of the M_w 7.7 event (shown by a white circle). Panels (a), (b), and (c) show the computed perturbations in the shear, normal, and Coulomb stresses, respectively, at the assumed depth of 5 km. Colors represent stress changes, in megapascals, on a logarithmic scale. The calculated Coulomb stress changes assume a coefficient of friction of 0.6. Panel (d) shows the orientation of potential receiver faults. Results for other possible fault orientations are shown in Supplementary Video S3.

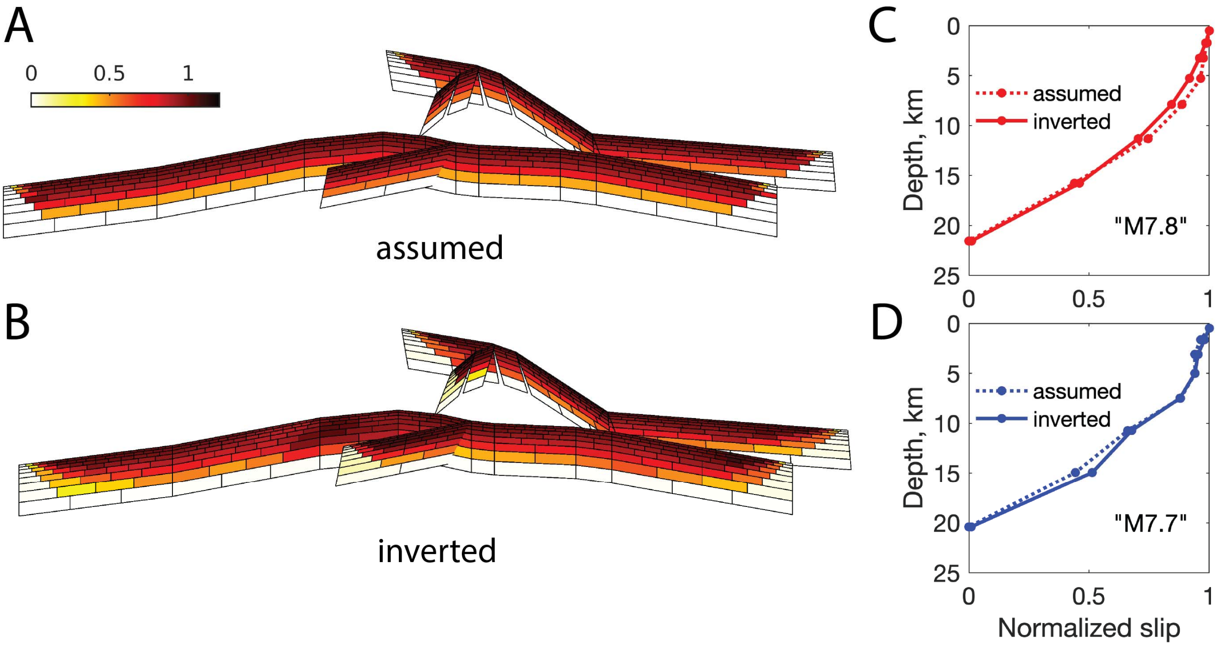

Fig. S28.
A synthetic test of the resolving power of our static slip model. We use the preferred fault geometry and assumed slip distribution, as shown in panel (a), to generate synthetic data at the same observation points that were used in our inversions. The resulting data set is then inverted using the same parameters as in inversions of actual data. The resulting slip distribution is shown in panel (b). Panels c and d compare the along-strike averaged normalized slip as a function of depth on faults representing the (c) M_w 7.8 and (d) M_w 7.7 ruptures. Note that the shallow slip is resolved reasonably well, and no apparent deficit is introduced due to some missing near-field data (Fig. S1).

Satellite Mode	Track Number	Preseismic Acquisition Date	Postseismic Acquisition Date
Sentinel-1	Ascending 14	2023/01/28	2023/02/09
Sentinel-1	Ascending 116	2023/02/04	2023/02/28
Sentinel-1	Descending 21	2023/01/29	2023/02/10
ALOS-2 Strip mode	Descending 78	2022/04/06	2023/02/08
ALOS-2 ScanSAR	Ascending 183	2019/09/18	2023/02/15
ALOS-2 ScanSAR	Ascending 184	2022/09/05	2023/02/20
ALOS-2 ScanSAR	Ascending 185	2022/09/10	2023/02/11
ALOS-2 ScanSAR	Descending 76	2022/09/11	2023/02/12
ALOS-2 ScanSAR	Descending 77	2022/09/16	2023/02/17
ALOS-2 ScanSAR	Descending 78	2022/09/07	2023/02/22

Table S1.
Coseismic Sentinel-1 and ALOS-2 SAR acquisitions used in this study.

Vp (km/s)	Vs (km/s)	Density (g/cm^3)	Thickness (km)
3.88	2.04	2.38	1
4.52	2.43	2.46	1
5.62	3.03	2.64	2
5.75	3.31	2.66	2
5.85	3.38	2.68	2
5.96	3.43	2.71	2
6.00	3.44	2.72	2
6.05	3.46	2.73	4
6.32	3.62	2.79	4
6.40	3.67	2.81	5
6.83	3.92	2.92	5
6.89	3.94	2.94	7
7.80	4.40	3.22	8
8.22	4.56	3.37	15
8.30	4.61	3.40	0

Table S2.
1D velocity structure used in this study. Model originally from Guvercin et al. (*23*). The density is derived following the Nafe–Drake empirical relationship (*111*).